Master of Science Degree in Aerospace Engineering

Academic Year 2024-2025

Graduate Session March-April 2025

Master of Science Thesis

Effect of an array of small-scale Helmholtz resonators on turbulent boundary layer flow

Supervisors:

Dr. Woutijn Baars

Ir. Abdelrahman Hassanein

Internal Supervisor:

Prof. Francesco Avallone

Student:

Edoardo Olivero

Abstract

Small-scale Helmholtz resonators embedded in a wall beneath a turbulent boundary layer can modify the energy of the turbulent velocity fluctuations when the resonator frequency is tuned in certain ways to the characteristic frequencies in the flow. This work experimentally investigates the impact of an array of small-scale Helmholtz resonators on a turbulent boundary layer, using particle image velocimetry and hot-wire anemometry. The specific aim of the study is to address whether the effect of a single Helmholtz resonator is amplified when multiple resonators are arranged in an array. In this investigation, we study a turbulent boundary layer flow at a friction Reynolds number of $Re_\tau \approx 2600$ using two different array configurations. Both configurations consist of resonators with an orifice diameter of $d^+ = 60$, but differ in the streamwise spacing between the spanwise rows of resonators. The spacing was designed with an attempt to achieve a strong interaction between the resonator-induced velocity fluctuations and natural turbulence dynamics. Changes in the mean flow were observed downstream of both configurations. However, differences in energy distribution across scales were evident only in the configuration with a higher density of resonators. This arrangement also led to a reduction in the skin friction coefficient in the wake of the final rows of resonators, extending up to $1000 l_\nu$ beyond the last resonator. This indicates a possible accumulation of the effect of a single small-scale resonator, when using an array.

Preface

This thesis is the end of a long journey started in 2019, a path full of emotions, positive and negative, but it has formed me a lot, and has taught me to overcome any difficulties, with method and perseverance.

I would like to thank my supervisor, Dr. Woutijn Baars, for welcoming me into his lab at TU Delft and for his continuous support throughout the entire research period. I am also sincerely grateful to my co-supervisor, Ir. Abdelrahman Hassanein, whose guidance has been invaluable at each stage of the project. Additionally, I would like to extend my thanks to Prof. Francesco Avallone for giving me the opportunity to carry out this thesis project abroad.

Finally, I would like to thank all the people who made this incredible journey possible. First and foremost, my parents and family, who have supported me at every moment. I am also deeply grateful to my girlfriend, who has always been by my side throughout these years. Lastly, I want to thank my friends, who have always been there for me whenever I needed help.

Edoardo Olivero
Delft, February 2025

Contents

List of Figures

List of Tables

Nomenclature

Acronyms

DEMO	Department of Electronic and Mechanical Development
DNS	Direct numerical simulation
DUBLF	Delft University Boundary Layer Facility
FOV	Field of view
HR	Helmholtz resonator
HWA	Hot wire anemometry
LSL	Low speed lab
PIV	Particle image velocimetry
TBL	Turbulent boundary layer

Greek Symbols

α	Stiffness spring constant
Δs	Displacement of the tracer particle
Δt	Time interval between the image pairs
Δx_i	Streamwise spacing between the spanwise rows of resonators
Δy	Position of the HWA probe with respect to the wall
δ	Boundary layer thickness
κ	Von Karman constant
λ_x	Wave length
$\lambda_{x,0}$	Wavelength converted from the resonance frequency
ν	Kinematic viscosity
ω	Angular frequency
$\phi_{u_i u_i}$	Spectral energy density

ρ	Fluid density
τ	Total shear stress
τ_w	Wall shear stress
ε	Pseudo-dissipation term
ξ	Damping constant

Latin Symbols

$\mathcal{F}[\cdot]$	Fourier transform
$\mathcal{P}$	Turbulent production term
$\overline{u'u'}$	Streamwise Reynolds stress
$\overline{u'v'}$	Shear Reynolds stress
$\overline{v'v'}$	Wall-normal Reynolds stress
$\tilde{p}_c$	Phase averaged cavity pressure
$\tilde{u}'$	Phase averaged streamwise velocity fluctuations
$\tilde{v}'$	Phase averaged wall-normal velocity fluctuations
a_0	Speed of sound
C	Coles constant
C_f	Skin friction coefficient
d	Orifice diameter of the Helmholtz resonator
d_w	Diameter of the wire of the HWA probe
D_x	Size of the FOV in the streamwise direction
D_y	Size of the FOV in the wall-normal direction
f_0	Resonance frequency of the Helmholtz resonator
F_{ext}	Driving force
H	Height of the test section
H_r	Input-output transfer kernel
H_r^{aco}	Input-output transfer kernel for the pure acoustic excitation
H_{HR}	Input-output transfer kernel for the Helmholtz resonator excited by the turbulent boundary layer flow
i	Imaginary unit

K	Mean streamwise kinetic energy
k	Turbulent kinetic energy
k_x	Wave number
L	Length of the test section
l	Orifice length of the Helmholtz resonator
l^*	Correction term for the resonance frequency equation of the Helmholtz resonator
l_w	Length of the wire of the HWA probe
L_x	Dimension of the Helmholtz resonator's cavity in the streamwise direction
L_y	Dimension of the Helmholtz resonator's cavity in the wall-normal direction
L_z	Dimension of the Helmholtz resonator's cavity in the spanwise direction
l_ν	Viscous length
M	Mass of the system in the mass-spring analogy
p	Pressure field
p_c	Cavity pressure
p_i	Inlet pressure
P_∞	Free-stream pressure
q	Turbulent fluctuations magnitude
Re_x	Local Reynolds number
Re_τ	Friction Reynolds number
$Re_{critical}$	Critical Reynolds number
s	Cross-sectional area of the orifice of the Helmholtz resonator
t	Time
t_ν	Viscous time scale
u	Streamwise velocity
U_c	Convective velocity
U_∞	Free-stream velocity
u_τ	Friction velocity

v	Wall-normal velocity
v_0	Resonator-induced velocity fluctuations
V_c	Cavity volume of the Helmholtz resonator
v_p	Tracer particle velocity
$v_{resultant}$	Resultant velocity fluctuations
v_{tbl}	Turbulent boundary layer velocity fluctuations
W	Width of the test section
w	Spanwise velocity
x	Streamwise direction
y	Wall-normal direction
z	Spanwise direction
Z_i	Acoustic impedance

Superscripts

$\cdot'$	Fluctuating field
$\cdot^*$	Complex conjugate
$\cdot^+$	Inner-scaled parameter
$\bar{\cdot}$	Mean field

Chapter 1

Introduction

Most flows encountered in practical applications are turbulent. These turbulent flows are present in various scenarios, from atmospheric flows around the Earth to blood circulation in human arteries. They also play a dominant role in numerous engineering applications, including flow over car bodies, aircraft wings and fuselages, fan blades, and ducts transporting liquids or gases. Approximately 25% of the energy consumed by industry and commerce is used to move fluids through pipes, canals, or vehicles through air and water. One of the most extensively studied cases of turbulent flow occurs when a fluid moves over a flat surface, leading to the development of a turbulent boundary layer. When a turbulent boundary layer forms over a surface, energy losses occur due to interactions between the wall-bounded flow and the surface itself, with about 25% of that energy dissipated due to turbulence near walls. From an environmental perspective, wall-bounded turbulence is responsible for roughly 5% of global CO_2 emissions caused by human activities. Modifying the amount of energy lost in such flows could therefore have a significant positive impact on both climate change mitigation and economic costs.

Over the past decades, various flow control methods have been explored to reduce skin friction drag exerted on the surface by the grazing, viscous flow. These strategies include passive approaches, such as surface texturing, riblets, and coatings, as well as active methods, such as flow injection, suction, and electromagnetic or plasma-based control. In this study, a passive method is investigated, specifically the use of a small-scale Helmholtz resonator as a meta-unit to attenuate turbulence fluctuations in the grazing flow, and thereby reduce the turbulent transport and potentially affect the skin friction drag.

Although numerous studies have examined the interaction between Helmholtz resonators and turbulent boundary layers, only a few have focused on small-scale units. Particularly noteworthy are the findings of Hassanein et al. (2024), who reported a reduction in the skin friction coefficient in the wake of a single small-scale resonator. Inspired by these findings, this study investigates, for the first time, an array of multiple small-scale resonator units, precisely tuned to interact with the most energetic fluctuations in the flow. The aim is to examine whether the results of Hassanein et al. (2024) can be reproduced when multiple resonators are employed, and whether the array of resonators can enhance the skin friction reduction.

1.1 Research Questions

To guide the research throughout all stages, key research questions were formulated to define the project's objectives. The goals of this study are distinctly divided into two main parts: the first focuses on the design strategy aimed to intensify the interaction between the resonators array and the turbulent boundary layer, while the second addresses the physical observations of how the array influences the flow above.

What are the best sizes of an array of Helmholtz resonators?

- What is the optimal streamwise spacing between spanwise rows of Helmholtz resonators to maximize their interaction with the flow?
- How does the spatial density of resonators within the array influence its impact on the turbulent boundary layer?

Does an array of multiple resonators enhance the performance of a single resonator?

- Considering an array of Helmholtz resonators, is there an accumulation of the single Helmholtz resonator effect configuration?
- How does the array of Helmholtz resonator change the global properties of the TBL?
- In previous works the presence of a single small-scale resonator has minimal effect on the mean velocity profile of the TBL. Can an array of Helmholtz resonators considerably affect the mean velocity profile?

Could an array of Helmholtz resonators work as an effective passive method for manipulating wall-shear stress?

1.2 Thesis Outline

This thesis begins with the fundamental concepts of the turbulent boundary layer in Chapter 2, discussing its characteristics, mean velocity and kinetic energy profiles, and the mechanisms governing turbulence production and dissipation. Sweep and ejection events, along with spectral analysis, are considered to understand the energy distribution within the flow. Following this, the focus shifts to the Helmholtz resonator in Chapter 3, reviewing previous studies on its excitation by a grazing turbulent boundary layer. The design of the resonator is introduced, including the calculation of its resonance frequency using a mass-spring analogy. Additionally, different excitation mechanisms are examined, distinguishing between pure acoustic excitation and the interaction with a turbulent boundary layer. The methodology and experimental setup are then described in Chapter 4, detailing the wind tunnel facility, the characteristics of both single small-scale resonator and the arrays, and the manufacturing process. Various measurement techniques, including microphone measurements, particle image velocimetry, and hot wire anemometry, are discussed in relation to their role in capturing relevant flow data. Chapter 5 presents the response of Helmholtz resonators to turbulent boundary layer excitation, analyzing velocity profile and phase-averaged flow fields at the resonance frequency. Mean flow measurements and the impact on the skin friction coefficient downstream of the resonator array are also examined. The findings are further explored in the discussion Chapter 6, evaluating their implications in the broader context of flow control strategies. Finally, the conclusion, in Chapter 7, summarizes the key outcomes of the study, highlighting its contributions and potential future research directions.

Chapter 2

Turbulent Boundary Layer

In the following chapter, the turbulent boundary layer (TBL) is described. We start, in Section 2.1, by explaining why a boundary layer emerges over a flat plate at zero incidence. In the same section, key mathematical tools and parameters are introduced to enable the analysis of this phenomenon. An analysis of the energy balance within the turbulent boundary layer is presented in Section 2.2, followed by the description of the sweep and ejection events in Section 2.4. In the next Section, 2.3, the mean field of the turbulent boundary layer is characterized by analyzing the streamwise mean velocity profile and the mean turbulent kinetic energy profile. Finally, the last Section 2.5 outlines the distribution of energy across different scales within the turbulent boundary layer.

2.1 Boundary Layer over a flat plate at Zero Incidence

Whenever a fluid flow interacts with a surface, such as the fuselage of an aircraft, the hull of a ship or the blade of a turbine, two distinct unequally large regions are identified. One thin layer close to the surface where the viscous effects are dominant, and a second larger layer where the viscous effects are neglected. Our focus will be on the thin layer close to the surface, known as boundary layer or frictional layer whose concept was introduced for the first time by Prandtl in 1904.

In this layer the velocity goes from zero at the wall, due to the no-slip condition, up to the free-stream velocity far from the wall. This layer is extremely important since it is the region of the boundary layer where all the energy losses occur due to the flow viscosity. The coordinate system for a boundary layer is typically a Cartesian system (x, y, z), where x is the streamwise direction (aligned with the mean flow), y is the wall-normal direction (perpendicular to the surface), and z is the spanwise direction (parallel to the wall and perpendicular to x). We will consider the simplest case of interaction between a surface and a flow: an incompressible, zero-pressure-gradient boundary flow over a smooth, flat plate, with a free-stream velocity U_∞ in the x-direction. The streamwise velocity at the wall is zero and the wall-normal and span-wise velocities as well. The flow is considered statistically steady in time relative to the wall and homogeneous in the span-wise z-direction. In this coordinate system, the flat plate is located in the x-z plane and is exposed to a uniform, non-turbulent velocity field along the x-axis, as depicted in the sketch in Figure 2.1.

To investigate the boundary layer development, in the x-direction on the flat plate,

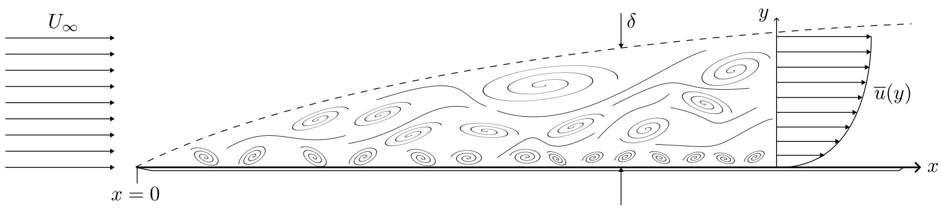

Figure 2.1: Two-dimensional turbulent boundary layer geometry.

we introduce the local Reynolds number defined as:

$$Re_x \equiv \frac{U_\infty x}{\nu} \tag{2.1}$$

where U_∞ is the free stream velocity and ν is the kinematic viscosity of the fluid. Knowing the value of this parameter, we can deduce information about the type of boundary layer at that point, specifically:

- for $Re_x < Re_{critical}$: the boundary layer is laminar, characterized by smooth and orderly flow;
- for $Re_x > Re_{critical}$: the boundary layer is turbulent, characterized by chaotic fluctuations and vortices.

The $Re_{critical}$ is the Reynolds number at which the boundary layer transitions from laminar to turbulent. For a flat plate, this parameter is approximately $Re_{critical} \approx 5 \cdot 10^5$. In this work we will focus on the turbulent part of the boundary layer because the vast majority of interactions between a surface and a fluid flow are turbulent, as reported by Anderson (1984). A zero pressure gradient is taken into account along the streamwise direction, therefore the free stream velocity is considered constant along the x-direction. The turbulent boundary layer, as mentioned before, is characterized by a highly unsteady flow field. It exhibits fluctuations in both pressure and three-dimensional velocity fields, which vary spatially and temporally. Using the Reynolds (1895) decomposition we get:

$$\begin{aligned} u(x,t) &= \overline{u}(x) + u'(x,t) \\ v(x,t) &= \overline{v}(x) + v'(x,t) \qquad p(x,t) = \overline{p}(x) + p'(x,t) \\ w(x,t) &= \overline{w}(x) + w'(x,t) \end{aligned} \tag{2.2}$$

where (u, v, w) are the components of the velocity field, t is the time coordinate, p is the pressure field, $\bar{\cdot}$ indicates the temporal average and u', v', w', p' indicate the fluctuating fields. The force interaction between the flow and flat plate itself is expressed by the total shear stress, which is defined as:

$$\tau(y) = \rho\nu\frac{\partial \overline{u}}{\partial y} - \rho\overline{u'v'} \tag{2.3}$$

where ρ is the fluid density. In Equation 2.3 the first term on the right-hand side is known as viscous stress and the second one is known as Reynolds stress, according to Pope (2000). At the wall, where $y = 0$, viscous stress is the most important component of the total shear stress and here the velocity fluctuations u' and v' are zero. We can define the wall shear stress as:

$$\tau_w = \rho\nu \frac{\partial \overline{u}}{\partial y}\bigg|_{y=0} \tag{2.4}$$

in the same way we can define the non dimensional parameter for the wall shear stress, known as the skin friction coefficient:

$$C_f \equiv \frac{\tau_w}{\frac{1}{2}\rho U_\infty^2} \tag{2.5}$$

This indicates that in the near-wall region, viscous effects dominate, making ν and τ_w crucial parameters for describing the behavior of the turbulent boundary layer. As result, the structures in the closest region to the wall are scaled using the viscous length, defined as:

$$l_\nu \equiv \frac{\nu}{u_\tau} \tag{2.6}$$

where u_τ is the friction velocity, defined:

$$u_\tau \equiv \sqrt{\frac{\tau_w}{\rho}} \tag{2.7}$$

The friction velocity and the viscous length are the scale factors for quantities in the near wall region. In our study we will also focus on the turbulent boundary layer features in the spectral domain, therefore is extremely important to define the time scale parameter:

$$t_\nu \equiv \frac{l_\nu}{u_\tau} \tag{2.8}$$

Their respective non-dimensional quantities are indicated by $\cdot^+$. In regions farther from the wall, the Reynolds stress is the most important component of the shear stress and the structures in this case are much larger, therefore the length scale parameter is the turbulent boundary layer thickness δ, defined as the y position where the local velocity is 99% of the free-stream velocity U_∞. Turbulent boundary layer thickness (δ) continuously increases in the streamwise x-direction. This is due to the transfer of momentum from the free stream to the boundary layer through turbulent mixing, as reported by Bailly and Comte-Bellot (2015). Regarding the time quantities also a time scale parameter δ/U_∞ is provided by Anderson (1984). Finally is defined the friction Reynolds number:

$$Re_\tau \equiv \frac{\delta u_\tau}{\nu} \tag{2.9}$$

which express the ratio between the inertial and viscous forces in a turbulent boundary layer.

2.2 Turbulence Production-Dissipation

The presence of flush-mounted resonators, in the wall under a turbulent boundary, layer affects the fluctuating field in the boundary layer itself, according to Hassanein et al. (2024) and Dacome et al. (2024). To explore how turbulence dynamics, within the boundary layer, is related to the velocity fluctuating fields, we will analyze the energy budget within a turbulent boundary layer. In this section, we will examine how turbulence is generated, how it transfers energy from large scales to smaller scales, and how it ultimately dissipates into heat. We start introducing the momentum equation of the Reynolds Averaged Navier-Stokes Equations with the approximation of turbulent boundary layer with zero-pressure gradient, as reported by Bailly and Comte-Bellot (2015):

$$\overline{u}\frac{\partial \overline{u}}{\partial x} + \overline{v}\frac{\partial \overline{u}}{\partial y} = \nu \frac{\partial^2 \overline{u}}{\partial y^2} - \frac{\partial \overline{u'v'}}{\partial y^2} \tag{2.10}$$

Following Renard and Deck (2016), the energy budget in a turbulent boundary layer can be expressed using the material derivative, defined as:

$$\frac{\overline{D}}{\overline{D}t} = \overline{u}\frac{\partial}{\partial x} + \overline{v}\frac{\partial}{\partial y} \tag{2.11}$$

This form does not include the temporal derivative term $\frac{\partial}{\partial t}$ because the mean field is steady. Additionally, using the definition of the total shear stress:

$$\frac{\tau}{\rho} = \nu \frac{\partial \overline{u}}{\partial y} - \overline{u'v'} \tag{2.12}$$

The momentum equation can be rewritten as:

$$\frac{\overline{Du}}{\overline{D}t} = \nu \frac{\partial^2 \overline{u}}{\partial y^2} - \frac{\partial \overline{u'v'}}{\partial y^2} = \frac{\partial}{\partial y}\left(\frac{\tau}{\rho}\right) \tag{2.13}$$

We can now obtain the budget of mean streamwise kinetic energy, defined as $K = \overline{u}^2/2$, multiplying the previous equation by $\overline{u}$:

$$\underbrace{\frac{\overline{D}K}{\overline{D}t}}_{A} = \underbrace{\frac{\partial}{\partial y}\left(\overline{u}\frac{\tau}{\rho}\right)}_{B} - \underbrace{\nu\left(\frac{\partial \overline{u}}{\partial y}\right)^2}_{C} + \underbrace{\overline{u'v'}\frac{\partial \overline{u}}{\partial y}}_{D} \tag{2.14}$$

On the left-hand side, term A, we have the rate of change of the mean streamwise kinetic energy K, while the right-hand side contains, in sequence: the viscous and turbulent diffusion of K, term B, the streamwise mean kinetic energy dissipation by effect of viscosity, term C and the *dissipation* of K through the production of turbulent kinetic energy, term D. This last term correspond to a transfer of kinetic energy to the fluctuating field and does not represent a true dissipation term, as the production of turbulent kinetic energy from the mean field is not *associated with irreversible entropy generation*, according to Renard and Deck (2016). The term D, therefore, represents the transfer of energy from the larger scales, present in the mean field, to the smaller scales within the fluctuating field. To prove the occurrence of this energy transfer we derive the budget of turbulent kinetic energy. To obtain this budget equation we derive the Navier Stokes Equations for the fluctuating fields subtracting the mean-field equations from the instantaneous ones, after we multiply the momentum equation, of the fluctuating field, by u', v', w' respectively and we take the average. The resulting budget equation is:

$$\frac{\overline{D}k}{\overline{D}t} = \mathcal{P} - \varepsilon + \nu\frac{\partial^2 k}{\partial y^2} - \frac{\partial}{\partial y}\left[\overline{v'\left(p + \frac{\rho}{2}q^2\right)}\right] \tag{2.15}$$

where k is the turbulent kinetic energy, defined as:

$$k = \frac{1}{2}\overline{q^2} = \frac{1}{2}\overline{(u'^2 + v'^2 + w'^2)} \tag{2.16}$$

and q represents the root mean square (RMS) of the velocity fluctuations or turbulent fluctuations magnitude. In equation 2.15, the left-hand side term represents mean-flow convection. On the right-hand side, $\mathcal{P}$ denotes the production term, ε represents the pseudo-dissipation, the third and fourth terms correspond to viscous diffusion and turbulent diffusion, respectively. By explicitly expressing the production term, we obtain:

$$\mathcal{P} = -\overline{u'v'}\frac{\partial \overline{u}}{\partial y} - (\overline{u'^2} - \overline{v'^2})\frac{\partial \overline{u}}{\partial y} \tag{2.17}$$

where the first term is the same found in equation 2.14, representing the energy transfer from larger scales to smaller scales. Whereas, the second term is usually neglected compared to the first one, as reported by Schlichting and Gersten (2016). We can explicit the pseudo-dissipation term as well:

$$\varepsilon = \nu\left[\overline{\left(\frac{\partial u'}{\partial x}\right)^2} + \overline{\left(\frac{\partial v'}{\partial y}\right)^2}\right] \tag{2.18}$$

this term represents the direct dissipation of turbulent fluctuations due to viscosity in internal energy. The turbulent kinetic energy budget represents the balance between four different contributions the convection, the diffusion, the dissipation and the production. The turbulent production term is typically positive, and can be referred to as *energy source*, in contrast to the dissipation term, which is generally negative and can be referred to as an *energy sink*. However, in some regions of the boundary layer, the production term can also become negative, indicating that energy is being transferred from the fluctuating field back to the mean field, as obsevred by Bailly and Comte-Bellot (2015). In the near-wall region the production and dissipation terms are the most significant: as described earlier, dissipation exceeds production very close to the wall, while in the buffer layer, production surpasses dissipation. In the log-region, the ratio between production and dissipation is approximately 1, indicating that turbulent kinetic energy is only transferred to adjacent regions. Finally, in the outer layer, the transport terms play a dominant role in balancing turbulent kinetic energy.

2.3 Turbulent Boundary Layer Mean Field

In this section is provided a description of the mean field of the turbulent boundary layer, paying attention at the mean velocity profile and at the mean turbulent kinetic energy profile.

2.3.1 Streamwise Mean Velocity Profile

The identification of distinct regions, within a turbulent boundary layer, is a significant aspect because each of these regions display different turbulence characteristics, as described by Pope (2000). In Figure 2.2 the mean velocity profile of a turbulent boundary layer over a smooth-flat-plate is depicted. By analyzing the mean

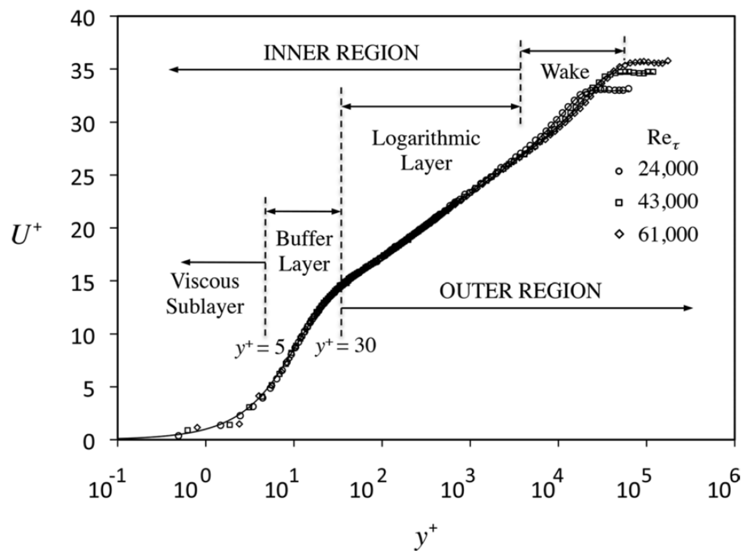

Figure 2.2: Mean velocity profile of a smooth-flat-plate turbulent boundary layer in log-linear coordinates with the law of the wall normalization. The data are plotted from Perlin et al. (2016) and represent three Reynolds numbers.

streamwise velocity profile, the inner region is the first one, it is located close to the wall ($y/\delta < 0.1/0.2$) and it is where turbulence production exceeds dissipation, as reported by Pope (2000). The inner region can be further subdivided into additional sub-regions:

- **Viscous Sublayer** ($0 \leq y^+ \leq 5$): where the viscous effects are more dominant than the turbulent ones and the velocity profile is linear, in according to Pope (2000):

$$u^+ = y^+$$

- **Buffer Layer** ($5 \leq y^+ \leq 30$): a buffer region between the viscous layer and the logarithmic layer.

- **Logarithmic Layer** ($30 \leq y^+ \leq 500$): in this region the velocity profile is logarithmic, in according to Pope (2000):

$$u^+ = \frac{1}{\kappa} \ln(y^+) + C$$

where $\kappa = 0.384$ is the Von Karman constant and $C = 4.17$ is the Coles constant, values proposed by Österlund et al. (2000). The main feature of this region is that the turbulence and viscous effects are balanced, therefore the energy is transferred from the large scale in the outer layer to the small scale in the inner layer where viscous dissipation occurs.

The outer layer situated further from the wall is characterized by dissipation rates that surpass turbulence production. Here, turbulence is sustained only through the kinetic energy transferred from the inner layers. The coherent structures in these regions are significantly different, with smaller scales closer to the wall and larger scales farther away. The outer region is located above $y/\delta = 0.2$ and it is characterized by turbulent momentum transfer dominance. In this region, the mean velocity profile diverges from the logarithmic law and approaches the free stream velocity, moreover the scale parameter is the boundary layer thickness δ. In Figure 2.2, the dependence of the mean velocity profile on the Reynolds number is illustrated. The inner region remains nearly unaffected by changes in Reynolds number of the flow, whereas the overlap layer expands.

2.3.2 Streamwise Turbulent Kinetic Energy Profile

To enhance the comprehension of the kinetic energy distribution along the wall-normal direction in the turbulent boundary layer the streamwise mean turbulent kinetic energy profile will be taken in account in this section. In this case we consider

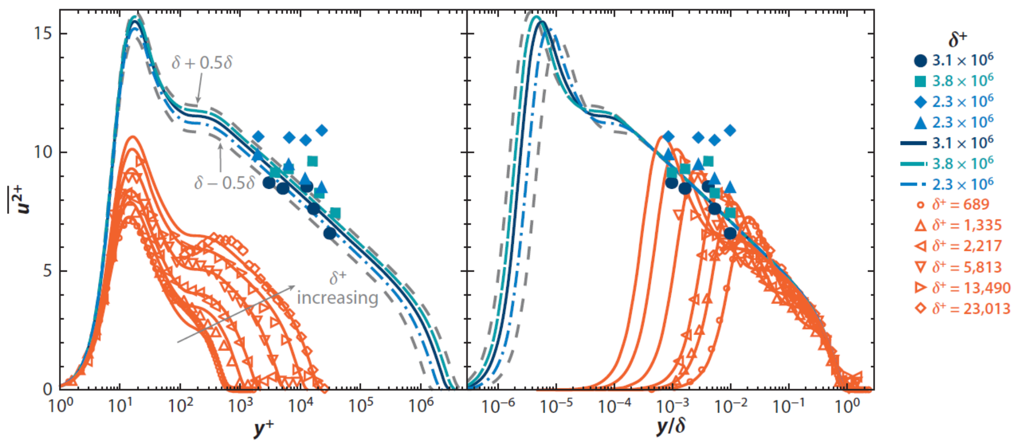

Figure 2.3: Turbulent kinetic energy profiles at different Reynolds numbers (indicated as $\delta^+ \equiv Re_\tau$ in this figure), plots from Smits et al. (2011).

only the fluctuations in the streamwise direction. As we can see in Figure 2.3 the turbulent kinetic energy profile present a peak in the buffer region of the inner layer, around $y^+ \approx 12$, as reported by Smits et al. (2011), in this point most of the turbulence activity is located and therefore most of the turbulent production in the boundary layer. To understand the presence of this peak, we can introduce the turbulent production term, which is discussed in Section 2.2:

$$\mathcal{P} = -\rho\overline{u'v'}\frac{\partial \overline{u}}{\partial y} \tag{2.19}$$

indeed, to achieve a high value of $\mathcal{P}$, it is necessary to have some distance from the wall so that the term $-\rho\overline{u'v'}$ (the Reynolds stress tensor) is not zero, which would otherwise result from the no-slip condition at the wall. However, as we move away from the wall, the velocity gradient $\partial\overline{u}/\partial y$ decreases, meaning that the ideal y-location cannot be too far from the wall, in according to Bailly and Comte-Bellot (2015). The same position of the turbulent kinetic energy peak has been found in various experiment and direct numerical simulations (DNS) such as Panton (2001), Renard and Deck (2016) and Smits et al. (2011). In the log-law region, the dominant energy balance in the flow occurs between the production and dissipation of turbulent kinetic energy. As the distance from the wall increases, the production of turbulent kinetic energy decreases. Consequently, in the outer region, the dominant balance shifts to one between dissipation and various transport terms.

2.4 Sweep and Ejection Events

Based on the production term, from equation 2.17, in the turbulent kinetic energy budget, four distinct situations can arise, depending on the velocity fluctuating fields. These are categorized as $Q1(+u', +v')$, $Q2(-u', +v')$, $Q3(-u', -v')$, and $Q4(+u', -v')$, commonly referred to as the quadrants of the Reynolds shear stress plane, in according to Wallace (2016). The $Q2$ and $Q4$ motions contribute positively to the production term in the turbulent kinetic energy budget, leading to an increase in turbulence production. In contrast, the $Q1$ and $Q3$ motions contribute negatively to the production term, resulting in a decrease in turbulence production. The events associate with the $Q2$ motion is called ejection which refer to the outward movement of low-speed fluid away from the wall in a turbulent boundary layer. They play a crucial role in the *bursting* process, which is a major driver of turbulence generation near the wall. Ejections make a significant contribution to both Reynolds stress and the production of turbulence, as reported by Robinson (1991). Another key contributor to turbulence production is the occurrence of sweep events, which are linked to the $Q4$ motion. These events involve the inward movement of high-speed fluid toward the wall, often including inrushes from the outer region of the boundary layer.

2.5 Spectral Analysis of the Turbulent Boundary Layer

Considering the spectral features of the Helmholtz resonators (HR), which will be the focus of our study, it is crucial to analyze the spectral characteristics of the turbulent boundary layer. The spectral energy density, indicated as $\phi_{uu}(k_x)$, allow us to identify the distribution of energy as a function of the wave number k_x. Figure 2.4 shows the premultiplied spectrum derived from the DNS data of turbulent channel flow conducted by Lee and Moser (2015), evaluated at various wall-normal positions. Two different peaks are present in this plot, the first one occurs at low-wavenumbers while the second occurs at high-wavenumbers. The presence of these two peaks highlights the bimodal characteristic of high Reynolds number turbulent flow. This separation of spectral peaks becomes noticeable for Re_τ values exceeding 1700, even though a $Re_\tau > 4000$ is proposed by Smits et al. (2011) to ensure a sufficient scale separation. Another way to observer the bimodal feature of the turbulent boundary layer is using contour plot of the premultiplied spectra $k_x^+ \phi_{uu}^+$ as function of the wall normal position (y^+) and the wave length (λ_x^+), defined as:

$$\lambda_x^+ = \frac{2\pi}{k_x^+} \tag{2.20}$$

These types of plots are presented in Figure 2.5 for various Reynolds numbers. Compared to the earlier plot in Figure 2.4, they enable us also to identify the wall-normal positions of the spectral peaks. The peak close to the wall, known as inner peak,

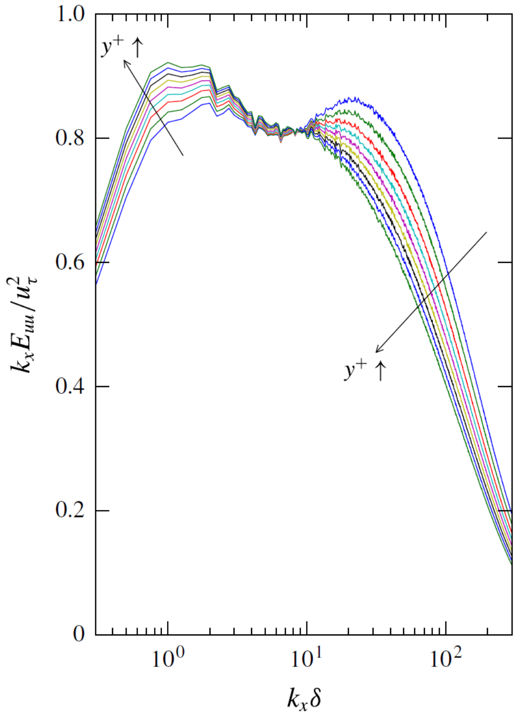

Figure 2.4: Premultiplied spectrum, $k_x^+ \phi_{uu}^+$, of the streamwise velocity fluctuations at $y^+ = 60 - 170$ ($Re_\tau = 5186$), DNS data by Lee and Moser (2015).

indicated with a white (+)-symbol, is normally located at ($y^+ \approx 15, \lambda_x^+ \approx 1000$) and it represents the point of maximum turbulence production for those Reynolds number values Hutchins and Marusic (2007). These figures also clearly show the emergence of a second distinct peak, as the Reynolds number increases, far from the wall normally known as outer peak, indicated with a black (+)-symbol and located at ($y/\delta \approx 0.06, \lambda_x/\delta \approx 6$). We can conclude, therefore, that at high Reynolds numbers, two distinct scales of separation between turbulence near the wall and turbulence farther from the wall become evident, as noted by Lee and Moser (2015).

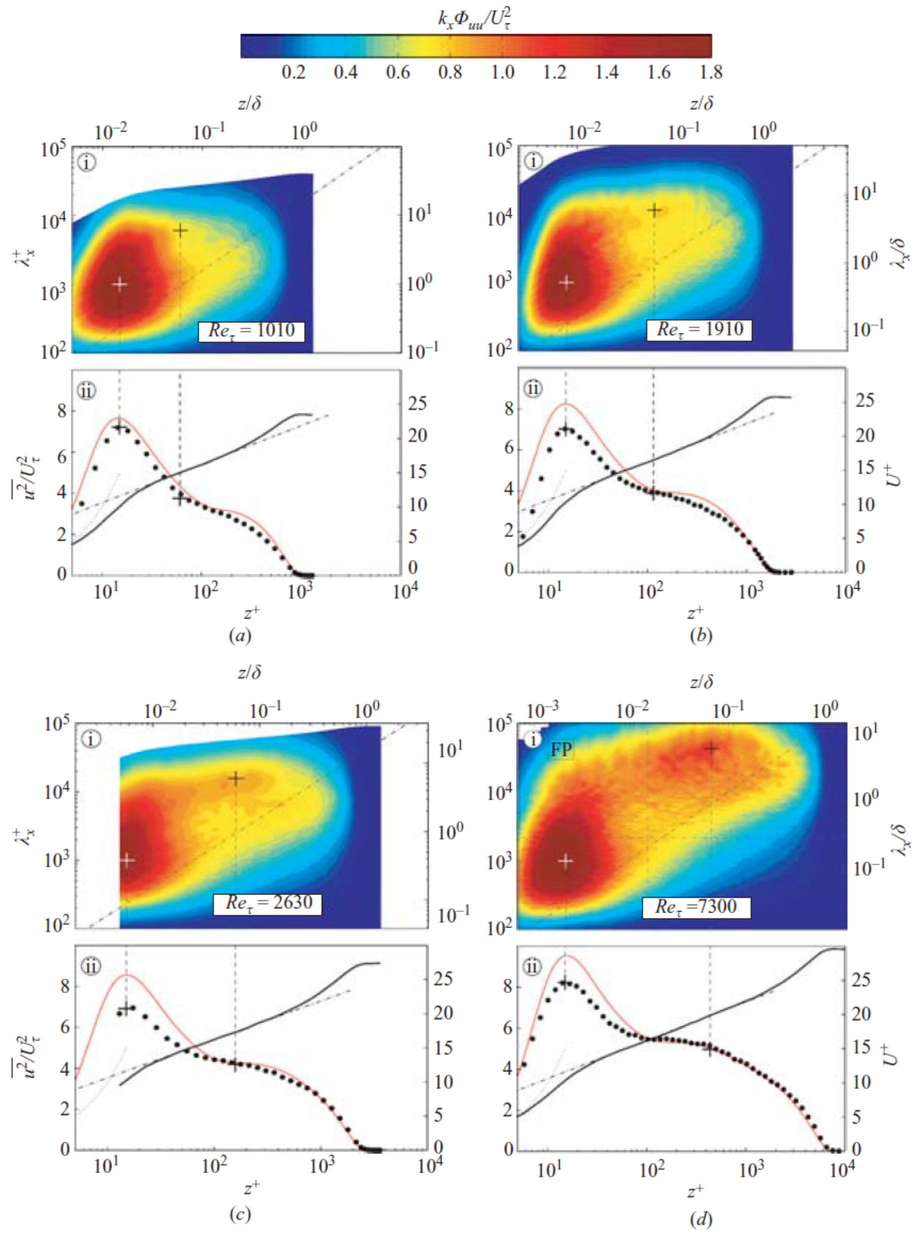

Figure 2.5: (i) Contour maps showing variation of one-dimensional pre-multiplied spectra with wall-normal position for (a) $Re_\tau = 1010$; (b) $Re_\tau = 1910$; (c) $Re_\tau = 2630$; (d) $Re_\tau = 7300$. (ii) Corresponding mean profiles of (●) streamwise turbulent kinetic energy, defined in 2.3.2, and (-) mean streamwise velocity. Dot-dashed line shows $\overline{u}^+ = (1/\kappa)\ln(z^+)+C$ (where $\kappa = 0.41$ and $C = 5.0$). Red line shows MK2003 formulation. Spectrograms from Hutchins and Marusic (2007).

Chapter 3

Helmholtz Resonator

This chapter introduces the Helmholtz resonator and its interaction with a turbulent boundary layer. In Section 3.1, the previous studies of Helmholtz resonators under a turbulent boundary layer are reviewed and is proposed an insight of our work, explaining the difference with the previous studies. In next Section 3.2 the geometrical features of the Helmholtz resonator are described, and its resonance behavior, in Section 3.3. Finally, the pure acoustic excitation and the excitation by a grazing turbulent boundary layer of a Helmholtz resonator are considered in Section 3.4.

3.1 Review of Works on the Excitation of a Helmholtz Resonator by a Grazing Turbulent Boundary Layer

Sound waves are the typical source of excitation for a Helmholtz resonator; however, turbulent flow across the orifice can also excite the resonator and the oscillations induced by the resonator can affect the turbulent flow itself. In this way the Helmholtz resonator can be used as a turbulence control device. This section reviews previous studies that have explored the use of the Helmholtz resonator as a passive turbulence control device, while also offering an overview of our work.

The concept of studying the interaction between a Helmholtz resonator and grazing flow was initially introduced by Panton and Miller (1975). In his work, a resonator was flush-mounted on the surface of a glider's fuselage. The resonance frequency of the resonator was set to match the peak of the pressure spectrum in the turbulent boundary layer, with the orifice dimensions of the resonator scaled to the same order of magnitude as the boundary layer thickness. Panton concluded his work arguing that *a strong excitation phenomenon occurs when the resonator and the boundary layer are tuned. This occurs when turbulent eddies of about twice the orifice diameter in size flow past the orifice and impose a frequency equal to one of the resonant frequencies of the resonator.*

In his subsequent study, Panton et al. (1987), he examined a row of Helmholtz resonators arranged in the spanwise direction, focusing on how the flow motions induced by the resonators affected the characteristics of the turbulent boundary layer. Velocity profiles at various streamwise positions revealed a decrease in momentum near the wall, with this momentum deficit gradually diminishing further downstream.

Another work was made by Flynn et al. (1989), who tested a row of resonators in the span-wise direction spaced by one boundary layer thickness. Different measurements were made in the streamwise direction and he concluded that *the resonators suck in high momentum fluid and expel low or zero momentum fluid into the flow.* This was stated based on the observation of a streamwise velocity defect accompanied by an increase in velocity fluctuations in both the streamwise and spanwise directions.

Another significant study is Ghanadi et al. (2014) in which 12 different Helmholtz resonator configurations were tested under a grazing turbulent boundary layer. Ghanadi's findings revealed that increasing the orifice diameter dimensions leads to higher pressure fluctuations within the cavity, while reducing the orifice thickness produces a similar effect. Additionally, resonators with longer orifices were found to induce greater wall-normal velocity fluctuations, enhancing the resonator's suction effect on the grazing flow.

All the works mentioned so far consider an orifice diameter relatively large to the one used in our work. In the following list all the diameters used are reported:

- Panton and Miller (1975): $d^+ = 400, 800$
- Panton et al. (1987): $d^+ = 687$
- Flynn et al. (1989): $d^+ = 687$
- Ghanadi et al. (2014): $d^+ = 250, 1600$

Another groups of works, instead, consider an orifice diameter comparable with the one used in our work. In the following list the works with diameter size comparable with our are reported:

- Dacome et al. (2024): $d^+ = 68, 102$
- Hassanein et al. (2024): $d^+ = 60$

The first study to take in account is the one made by Dacome et al. (2024), where orifice with two different diameters, $d^+ = 68, 102$, were used. Dacome et al. (2024) concludes that although individual miniature Helmholtz resonators show promise in influencing turbulent boundary layer flow, their ability to attenuate large-scale energy remains limited. The study recommends that future research should explore interconnected HR networks to achieve more substantial flow control effects, including reductions in skin friction.

In conclusion, Hassanein et al. (2024) study, conducted with an orifice diameter of $d^+ = 60$, is noteworthy as it aimed to elucidate how the resonator influences turbulence within the boundary layer across various scales. Specifically Hassanein et al. (2024) found that the resonator amplifies the fluctuations in the resonance frequency, whereas attenuates the fluctuations in the sub-resonance frequencies.

As proposed by Hassanein et al. (2024) and Dacome et al. (2024) our research considers a bi-dimensional array of Helmholtz resonators to investigate whether the effects observed in single-resonator configurations are amplified.

3.2 Introduction to Helmholtz Resonator

A Helmholtz resonator is an acoustic device that consists of a rigid-walled cavity filled with a compressible fluid, connected to its surroundings through a short orifice. The Helmholtz resonator resonates at a particular frequency, known as the resonance frequency. This device is often employed to reduce acoustic intensity within pipelines, where viscous dissipation within the cavity attenuates acoustic intensity due to velocity gradients, as reported by Kinsler et al. (1999). When operating near

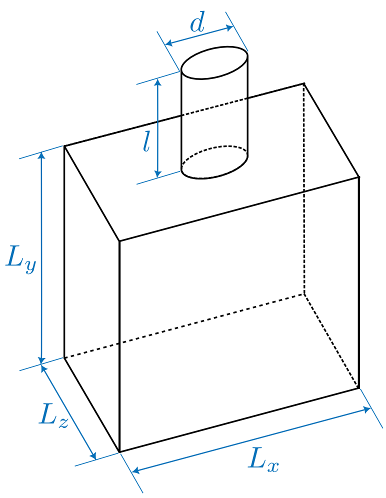

Figure 3.1: Three-dimensional Helmholtz resonator sketch.

the resonance frequency, small disturbances at the neck's inlet can lead to significant oscillations within the cavity, resulting in substantial acoustic intensity reduction. The resonant frequency of a Helmholtz resonator can be calculated based purely on its geometric properties. In the following section, a method utilizing a mass-spring system is introduced to determine the resonance frequency. A Helmholtz resonator is fully described by three dimensions: the orifice length l, the orifice diameter d and the cavity volume V_c, this means that the shape of the cavity doesn't affect the physical properties of the resonator. For instance in our case the cavity has a rectangular cross-section, therefore it is characterized by three dimensions in the three spatial directions L_x, L_y and L_z.

3.3 Calculation of the Resonance Frequency of a Helmholtz Resonator with the Mass-Spring Analogy

To compute the resonance frequency of the Helmholtz resonator it may be considered analogous to a mechanical system of a mass on a massless spring, as proposed by Alster (1972). The mass of the fluid in the neck of the resonator acts as the oscillating

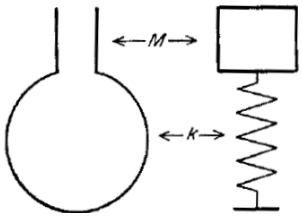

Figure 3.2: Mass-spring analogy of a Helmholtz resonator (in this schematic the stiffness spring constant is k instead of α). Schematic taken from Alster (1972).

mass in the analogy, as shown in the simple sketch in Figure 3.2. When an external pressure wave or grazing flow excites the resonator, this mass of air moves back and forth within the neck. The compressibility of the fluid within the cavity provides the spring-like restoring force. As the air in the neck moves inward, it compresses the air within the cavity. This compressed air then acts to push the air in the neck back outward. Just like a mass-spring system, a Helmholtz resonator has a natural frequency at which it will oscillate most readily. This resonance frequency is determined by the mass of the air in the neck and the stiffness (compressibility) of the air in the cavity. The resulting second order differential equation for the forces equilibrium is:

$$Mx'' + \alpha x = 0 \tag{3.1}$$

and the resonant frequency formula of this system is the solution of the previous equation:

$$f_0 = \frac{1}{2\pi}\sqrt{\frac{\alpha}{M}} \tag{3.2}$$

In this case, the mass in the mass-spring system corresponds to the air within the orifice, and it is defined as:

$$M = \rho s l \tag{3.3}$$

where ρ represents the density of the fluid (air, in this case), l is the length of the orifice, and $s = \pi(d/2)^2$ is the cross-sectional area of the orifice. The stiffness of the air, represented by the spring constant α in the mechanical system, given by Kinsler et al. (1999) is:

$$\alpha = \frac{\rho a_0^2 s^2}{V_c} \tag{3.4}$$

where a_0 is the speed of sound. This stiffness value, α, accounts for the compressibility of the air within the resonator cavity. The resulting resonance frequency equation is:

$$f_0 = \frac{a_0}{2\pi}\sqrt{\frac{s}{V_c l}} \tag{3.5}$$

Considering the effect of the spring's mass, a mass end correction term has been proposed by Ingard (1953), in detail we must add a correction term l^* to the orifice length:

$$l^* = 0.48\sqrt{s}\left(1 - 1.25\frac{d}{\sqrt{L_x L_z}}\right) + 0.48\sqrt{s} \tag{3.6}$$

moreover another correction to the resonance frequency equation has been proposed by Panton and Miller (1975), adding the correction term $\frac{1}{3}L_y^2/s$ to the denominator in the equation 3.5. Therefore, the resulting corrected equation for the resonance frequency of a Helmholtz resonator is:

$$f_0 = \frac{a_0}{2\pi}\sqrt{\frac{s}{V_c(l+l^*) + \frac{1}{3}\frac{L_y^2}{s}}} \tag{3.7}$$

3.4 Excitation of a Helmholtz Resonator

In Section 3.3, the resonance frequency of the Helmholtz resonator is derived using the mass-spring analogy, as outlined by Alster (1972) work. A homogeneous dynamical system has been taken in account for the analogy, leading to the formulation of the second-order differential equation 3.1. In this section, we take a step further by moving beyond the homogeneous dynamical system, instead, we will analyze an excited system subjected to an external driving force F_{ext}, as referred by Kinsler et al. (1999). In Sub-Section 3.4.1 the pure acoustic excitation case is considered, whereas in the Sub-Section 3.4.2 the excitation by a grazing turbulent boundary layer is reviewed.

3.4.1 Pure Acoustic Excitation of a Helmholtz Resonator

In this frame a pure acoustic excitation is considered, in absence of any cross-flow. The driving force is therefore a sound pressure wave expresses by Kinsler et al. (1999) as:

$$F_{ext} = spe^{i\omega t} \tag{3.8}$$

where p is the intensity of the sound pressure wave, $i = \sqrt{-1}$ is the imaginary unit, ω is the angular frequency and t is the time unit. The excitation of the Helmholtz resonator occurs when the angular frequency of the incident sound pressure wave is equal to the resonance frequency f_0 of the resonator. To study the response of the resonator to the acoustic signal the input-output transfer kernel H_r is introduced, as proposed by Dacome et al. (2024). H_r expresses the relation between the inlet pressure p_i and the pressure inside the cavity p_c. The gain and phase equations of H_r are respectively:

$$|H_r(f)| = \left[\left(1-\left(\frac{f}{f_0}\right)^2\right)^2 + \left(2\xi\frac{f}{f_0}\right)^2\right]^{-1/2} \tag{3.9}$$

$$\varphi[H_r(f)] = -\tan^{-1}\left[\frac{2\xi\,(f/f_0)}{1-(f/f_0)^2}\right] \tag{3.10}$$

where ξ is the damping constant. The function H_r^{aco} for the pure acoustic excitation scenario, can be inferred starting from the pressures signals p_c and p_i using the equation:

$$H_r^{\mathrm{aco}} = \frac{\langle P_c(f)P_i^*(f)\rangle}{\langle P_i(f)P_i^*(f)\rangle} \tag{3.11}$$

where numerator is the input-output cross spectrum and the denominator is the input spectrum. In equation 5.1 the capital symbols indicate the Fourier transform, e.g. $P_c(f) = \mathcal{F}[p_c(t)]$, and the superscript $\cdot^*$ indicates the complex conjugate. Another function useful to describe the response of a Helmholtz resonator is the acoustic impedance. A simple acoustic system, which can be analyzed using a mechanical analogy, it can also be represented as an electrical circuit, as described in Kinsler et al. (1999). In this representation, the fluid motion corresponds to the electrical current, while the pressure difference between two points is analogous to the voltage difference across two points in the circuit. Thus, we can express the acoustic impedance at the neck inlet of the Helmholtz resonator, as reported by Dacome et al. (2024), by:

$$Z_i \equiv \frac{P_i(f)}{V_i(f)} \tag{3.12}$$

where $V_i(f) = \mathcal{F}[v_i(t)]$ is the wall-normal velocity at the neck inlet of the resonator. In Figure 3.3 we can observe the response of the Helmholtz resonator to a pure

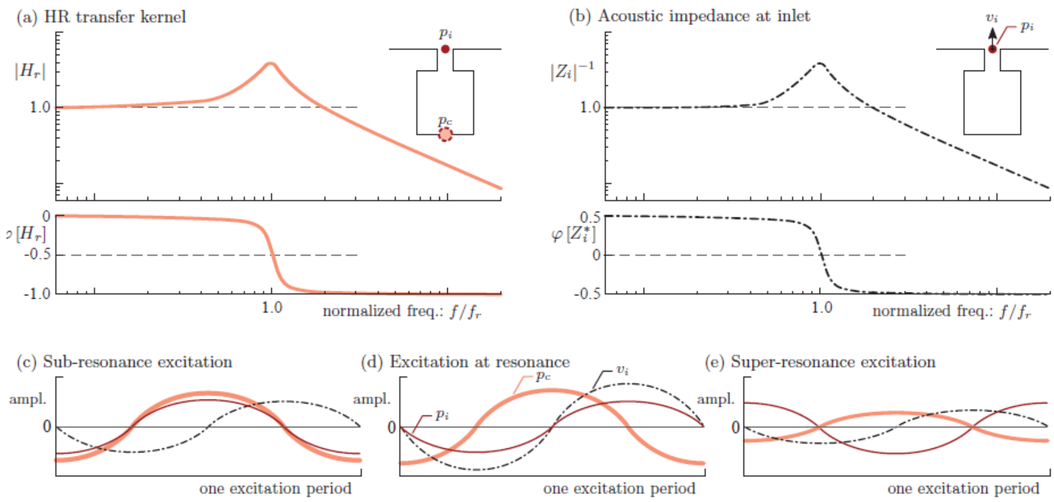

Figure 3.3: Bode plots of H_r (a) and acoustic impedance (b) in the case of pure acoustic excitation. Plots of pressure and velocity at the neck inlet and pressure at the cavity of one excitation period in the sub-resonance case (c), resonance case (d) and super-resonance case (e). Plot taken from Dacome et al. (2024).

acoustic excitation. Observing the amplitude plots of the transfer kernel and the impedance is clear the presence of a signal amplification when the Helmholtz resonator matches the resonance frequency f_0. Additionally, an important remark is the phase shift in the transfer kernel and the impedance when super-resonance frequencies are taken into account, as illustrated in the phase plot shown in Figure 3.3 (a,b). Finally, as reported by Dacome et al. (2024), the presence of the Helmholtz resonator embedded in the wall under a turbulent boundary layer changes the wall-impedance, thereby affecting the dynamics of the grazing flow.

3.4.2 Excitation of a Helmholtz Resonator by a Grazing Turbulent Boundary Layer

When a Helmholtz resonator is located beneath a turbulent boundary layer two different energy sources that excite the resonator can be identified.

- The first energy source is the shear layer separation that occur in the inlet of the orifice. The resonance frequency, used to tune the resonator, is taken from the Kelvin-Helmholtz instabilities of the vortices which originate from the orifice inlet. This scenario has been widely discussed by Ghanadi et al. (2014), Panton and Miller (1975), Panton et al. (1987), Flynn et al. (1989) where the orifice diameter was $d^+ \approx 200 - 2000$. However, this method of excitation is not elaborated on in this work, as a different orifice diameter will be employed in our study.

- The second energy source capable of exciting the resonator is the most energetic frequency of pressure fluctuations within the turbulent boundary layer. In this scenario, as reported by Dacome et al. (2024), *small-scale* resonators are considered, characterized by a neck orifice diameter on the order of $\mathcal{O}(10l_\nu)$. This latest case is the foundation of our work and will be therefore discussed in the this section.

In turbulent boundary layer flows velocity and pressure fluctuations exhibit a broad-band spectrum, therefore can be considered as pure acoustic excitation for Helmholtz resonators. The pressure fluctuations in the turbulent boundary layer act as an external driving force that excites the Helmholtz resonator, as discussed in Section 3.4.1 for pure acoustic excitation. This type of excitation process has been explored in various studies Dacome et al. (2024) and Hassanein et al. (2024). The latter investigated the interaction between a single resonator and a turbulent boundary layer, hypothesizing that pressure fluctuations drive the resonator while wall-normal velocity fluctuations represent its response.

Based on this premise, the frequency-dependent impedance of the Helmholtz resonator can be defined to quantify its response—represented by wall-normal velocity fluctuations—to pressure fluctuation excitation. Then three different case are taken into account: the sub-resonance case, the resonance case and the super-resonance case, considering the resonator tuned with the frequency peak of the pressure fluctuations spectrogram.

In Figure 3.4 are depicted these three different scenarios, in the case of sub-resonance the resonator-induced fluctuations (v_0) are in phase opposition with the incoming turbulent boundary layer fluctuations (v_{tbl}), resulting in an attenuated resultant velocity ($v_{resultant}$). In the resonance case, the turbulent boundary layer fluctuations and the resonator-induced fluctuations are in quadrature, leading to an amplification of the resultant velocity fluctuations. Lastly, in the super-resonance scenario, the two velocity fluctuations are in phase alignment; however, due to the viscous damping at those frequencies, the amplification of the resultant velocity is lower than in the resonance case.

This process, called *Resonance-Turbulence Interaction Mechanism* by Hassanein et al. (2024), has been described for the single-resonator configuration, the goal of this work is to figure out if the same effect may be identified in a multi-resonator configuration.

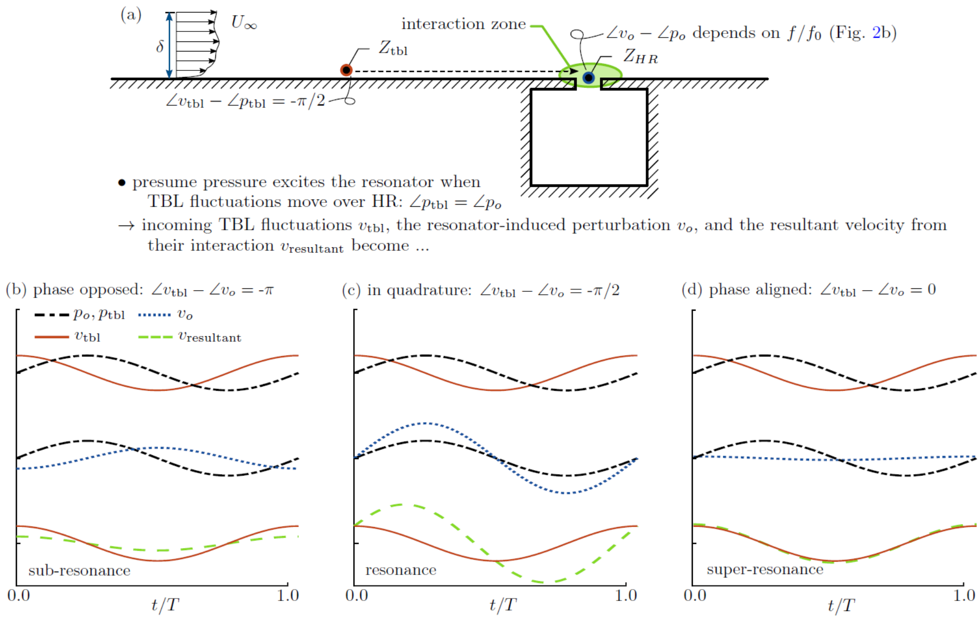

Figure 3.4: (a) Schematic of the Helmholtz resonator under the turbulent boundary layer. (b,c,d) Harmonic fluctuations over one period. Plot taken from Hassanein et al. (2024).

Chapter 4

Methodology and Design of the Experimental Setup

In this chapter the wind tunnel facility used for the experiments is described, in Section 4.1. Secondly, an insight on the experimental setups employed during the campaign, focusing on the design process of the small-scale resonator unit and on the different configurations, is presented in Section 4.2. Finally, in the last Section 4.4, the measurements techniques used in the experiments are described.

4.1 Wind Tunnel

The experiments were carried out in the Delft University Boundary Layer Facility (DUBLF) in the Low Speed Laboratory (LSL) at Delft University of Technology. It is a to-be closed-return wind tunnel, but in our case has been used in an open-loop configuration generates flow using a single axial fan and is designed for studying turbulent boundary layer regimes.

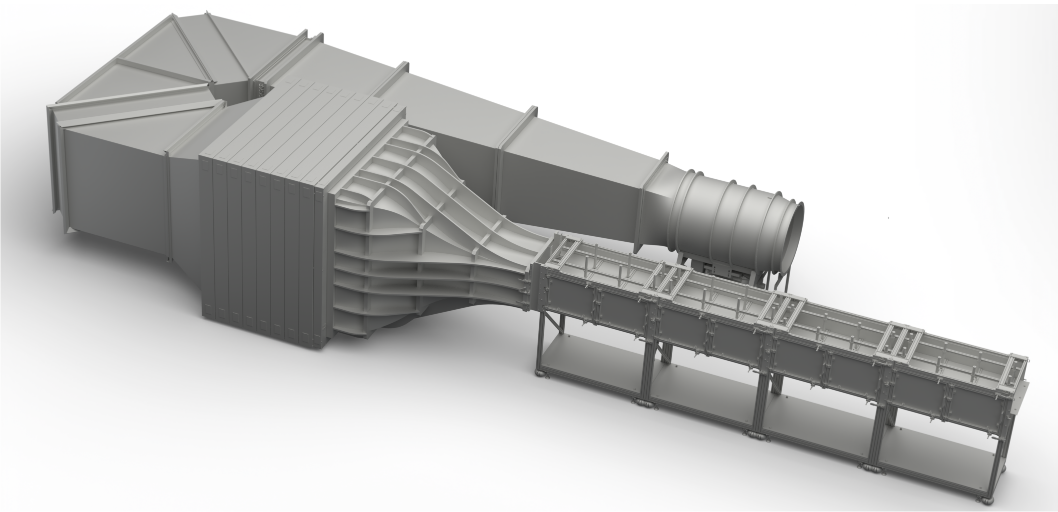

Figure 4.1: Delft University Boundary Layer Facility at the Low Speed Lab of Delft University of Technology.

The TBL develops on a plexiglass plate, which is the floor of a test section train measuring approximately $L\times W\times H \approx 0.5\,\mathrm{m}\times 0.9\,\mathrm{m}\times 0.6\,\mathrm{m}$. The test sections feature also a flexible ceiling, designed to maintain the zero-pressure-gradient condition, within the TBL. To force the transition to the turbulent regime, a strip of P-40 grain sandpaper is placed on all the sides at onset of the test section train. As shown Figure 4.1, the test section train is composed by four different sections, with the experiments conducted in the last one to ensure the development of a fully turbulent boundary layer. This section features a flat plate with dimensions $L \times W = 600$ mm $\times$ 220 mm, which can be replaced by a custom flat plate outfitted with the experimental setup. In our experiments, the free-stream velocity was set to $U_\infty = 10$ m/s. The turbulent boundary layer was characterized by a friction Reynolds number of approximately $Re_\tau \approx 2590$, a friction velocity of $U_\tau \approx 0.366$ m/s, and a viscous length of about $l_\nu \approx 41.52$ μm. Additionally, the boundary layer thickness was measured to be $\delta \approx 106$ mm. A summary of all these turbulent boundary layer parameters is provided in Table 4.1, while the mean streamwise velocity profile and the Reynolds stress profiles of the turbulent boundary layer are provided from hot-wire data and particle image velocimetry measurements.

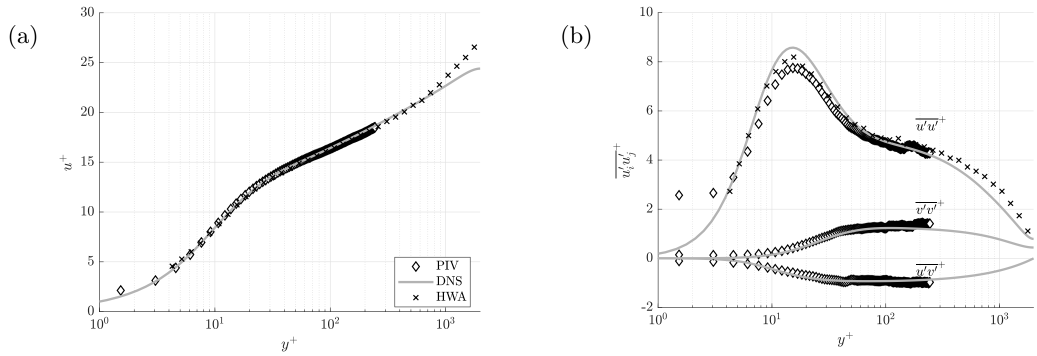

Figure 4.2: Comparison between the streamwise mean velocity profiles (a) and the Reynolds stress profiles (b) from PIV, HW and DNS data from Lee and Moser (2015) at $Re_\tau \approx 2000$.

Table 4.1: Characteristics of the turbulent boundary layer generated in the wind tunnel, as inferred from the hot-wire velocity profile across the entire turbulent boundary layer.

U_∞ (m/s)	Re_τ	δ (mm)	u_τ (m/s)	l_ν (μm)	t_ν (μs)
9.98	2511	106	0.36	42.5	118.4

4.2 Design of the Experimental Setup

This section presents and discusses the decisions involved in sizing the experimental setup. Specifically, Section 4.2.1 focuses on the sizing process of the small-scale resonator unit, while Section 4.2.2 details the design strategy for the array configurations.

4.2.1 Characteristics of the Single Helmholtz Resonator

The sizing process for the small-scale resonator unit aimed to create a meta-unit that could efficiently interact with the smaller scales within the TBL, as previously studied by Hassanein et al. (2024) and Dacome et al. (2024). Therefore, precise determination of each parameter's dimensions is essential for achieving the desired impact on the structures in the near-wall region of the TBL and modifying its behavior. The aim of the orifice design process is to enhance the interaction between the resonator and the flow, typically to maximize energy transfer between a specific turbulent scale and the resonator. The sizing of the orifice can be seen as the spatial tuning of the small-scale resonator unit. The selected orifice diameter was $d^+ = 60$, which has been found to be an effective size for attenuation of sweep events in a turbulent boundary layer accordingly to Silvestri et al. (2018). In particular the size of $d^+ = 60$ is half of the turbulent structure that excite the resonator, for instance the characteristic eddy size. This design strategy was first proposed by Panton and Miller (1975) and then adopted by several authors Hassanein et al. (2024), Dacome et al. (2024) and Silvestri et al. (2018). This choice represents a compromise between larger values, which enhance interaction with the TBL, and smaller values, which minimize the increase in pressure drag.

Another key parameter in the sizing of the small-scale resonator unit is the orifice length, which was set equal to $l^+ = 80$. This value is adopted by Dacome et al. (2024) and Hassanein et al. (2024), with the intention of minimizing viscous dissipation within the orifice, thereby enhancing resonance.

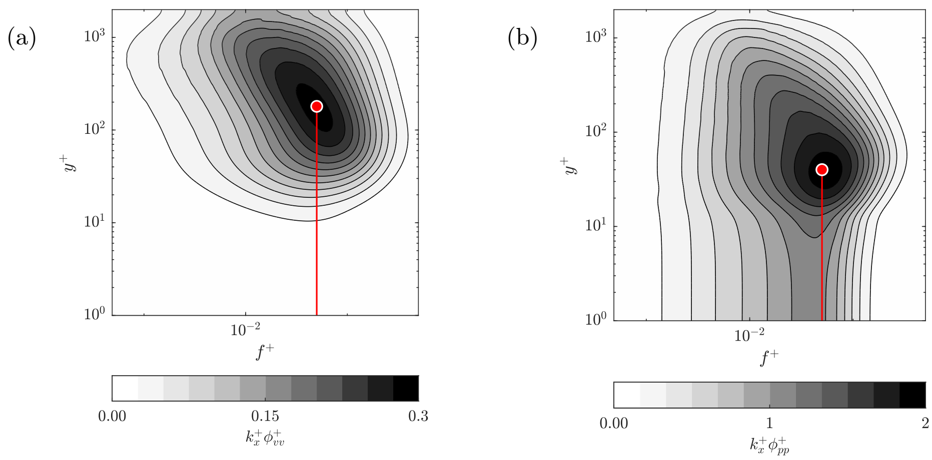

Figure 4.3: (a) Wall-normal velocity fluctuations spectrogram and (b) pressure fluctuations spectrogram. The vertical red lines indicate the frequency of the peak $f^+ \approx 0.04$. Spectrogram from turbulent channel flow DNS data of Lee and Moser (2015) at $Re_\tau \approx 2000$.

By adjusting the orifice sizing, we influenced the spatial tuning of the small-scale resonator unit. Similarly, we can consider the temporal tuning of the resonator by matching its resonance frequency with the most energetic turbulent structures within the TBL. In this case, the key characteristic of interest is the cavity volume. It determines the resonator's resonance frequency, as discussed in Section 3.4.2. In our specific case, the cross-sectional area of the cavity is fixed, meaning the cavity volume and, consequently, the resonance frequency of the resonator depend solely on L_y, the cavity depth. The resonance frequency was selected to match the peak frequency of the pressure spectrum, which coincides with the peak frequency of the wall-normal velocity fluctuations spectrum and is given by $f_0^+ = 0.04$, as shown in Figure 4.3. Although all the experiments were conducted with the resonance frequency fixed at $f^+ = 0.04$, the setup allowed for adjustments of the cavity depth length to achieve the desired resonance frequency even after the manufacturing. This design choice aimed to provide tolerance for the frequency value, enabling corrections if discrepancies were identified during measurements with the microphones or allowing the selection of different resonance frequency values in further experiments. To enable this adjustment, each cavity was filled with water to an adjustable level, which was pumped into the bottom of the cavities. In Table 4.2 are summarized all the small-scale resonator unit dimensions in millimeters and in plus unit.

Table 4.2: Characteristics of the small-scale resonator unit.

d^+	d (mm)	l^+	l (mm)	L_x^+	L_x (mm)	L_z^+	L_z (mm)	L_y^+	L_y (mm)
60	2.50	80	3.33	135	5.38	490	19.57	3500	140

4.2.2 Characteristics of the Helmholtz Resonator Array Configurations

After defining the size of the small-scale resonator unit, the next step was to identify the optimal arrangement of the resonator units in an array configuration. In this design process, the key parameter was the streamwise spacing between the rows of resonators, as this parameter is expected to influence the interaction between the array and the coherent turbulent structures within the TBL. Therefore, the streamwise spacing between the rows of resonators affects the spatial tuning of the array. To find out the best way to size the streamwise distribution of resonators, it was decided to use as reference distance for the spanwise resonators' rows the design resonance frequency f_0 converted to a streamwise wavelength:

$$\lambda_{x,0}^+ = \frac{U_c^+}{f_0^+} = 250 \tag{4.1}$$

where $U_c^+ = 10$, in according to Liu and Gayme (2020), is the convective velocity of the turbulent structures of the TBL close to the wall ($y^+ < 10$). The decision regarding the streamwise spacing between the different rows of resonators was also influenced by the need to avoid an excessive density of resonators on the plate, which could lead to a significant increase in pressure drag. Two different configurations were considered, in the first configuration (Config1), the streamwise spacing between the rows (Δx_1^+) was set equal to the characteristic wavelength of the most energetic coherent structures in the turbulent boundary layer (TBL), $\Delta x_1^+ = \lambda_{x,0}^+ = 250$. In the second configuration (Config2), the spacing was set twice the characteristic wavelength, $\Delta x_2^+ = 2\lambda_{x,0}^+ = 500$. On the other hand, the spanwise distance between the resonator rows was chosen based on the geometric constraints dictated by the dimensions of the interchangeable flat plate used in the wind tunnel. The aim was to maximize the number of resonators in the spanwise direction while maintaining a sufficient wall thickness between the resonator cavities to ensure structural rigidity.

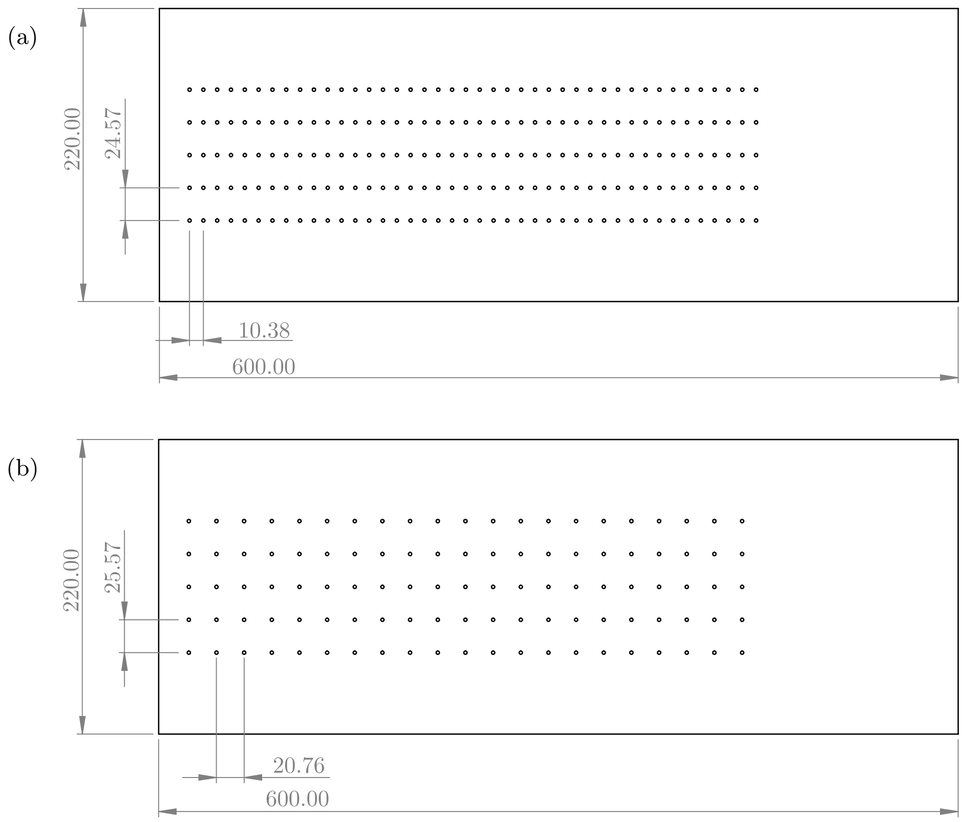

Figure 4.4: (a) Sketch of the top plate for configuration 1, where $\Delta x_1^+ = \lambda_{x,0}^+$. (b) Sketch of the top plate for configuration 1, where $\Delta x_2^+ = 2\lambda_{x,0}^+$. All dimensions are in millimeters.

Figure 4.4 presents a top view of the sketches of the flat plates used for the two configurations. In both plates configurations, an empty space of approximately 1.5δ is included to ensure the development of the flow downstream of the array and to enable HW measurements during the experiments.

4.3 Manufacturing Process of the Experimental Setup

The assembly of the experimental setup consists of different parts, presented in the list below:

- top plate
- cavities box
- microphone plates
- Festo adapters

- plastic pipes
- syringes

The top plates were manufactured by the Department of Electronic and Mechanical Development (DEMO) of the TU Delft in anodized black aluminum, to ensure a smooth surface on the upper side and also minimizing laser reflections in the orifices during particle image velocimetry (PIV) measurements. In Figure 4.5 a photo of the top plate for the configuration 1 installed in the test section is shown.

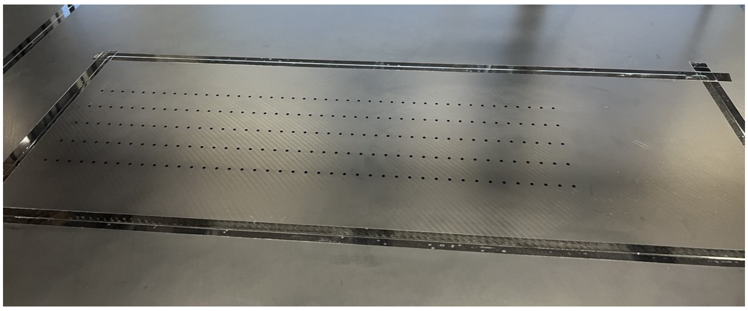

Figure 4.5: Top plate of the configuration 1.

The cavities box, which is the part located beneath the top plate housing all the resonator cavities, was 3D printed by the Bambu Lab X1E printer, present in the workshop of the LSL, using Polylactic Acid (PLA). By 3D printing the cavities boxes, we were able to minimize manufacturing costs, ensure good wall rigidity within the cavities and reducing design constraints, thanks to the flexibility offered by 3D printing technology. To ensure waterproofing of the cavities, the dichtol AM Hydro sealer was applied to the final model. At the bottom of the box, holes were positioned to accommodate the Festo adapters, which were screwed in place. These adapters enable the connection to syringes, allowing water to be pumped into the cavity bottoms to regulate their volumes. Each box was 3D printed in two separate parts due to the size limitations of the 3D printer. In Figure 4.6, three sides of one part of the box are shown.

(a) (b) (c)

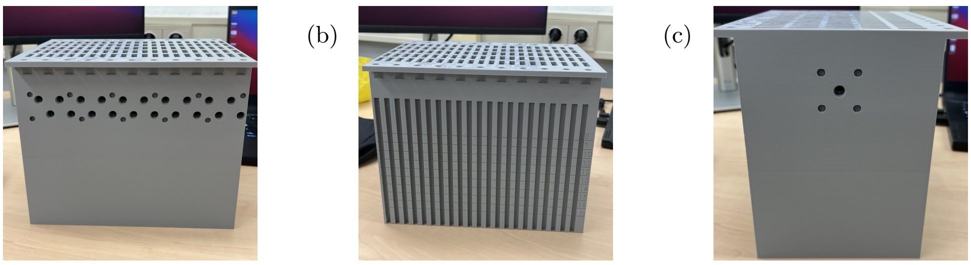

Figure 4.6: One part of the cavities box for the configuration 1. (a,c) Side where the microphones were installed. (b) Side where the transparent tubes were mounted to monitor the water level inside the cavities.

After manufacturing, the cavity box and the top plate were screwed together for each configuration. To prevent air leakage at the contact surface between the two parts vacuum grease was applied to both surfaces before assembly. In Figure 4.7 a render of the assembly for the configuration 1 is shown.

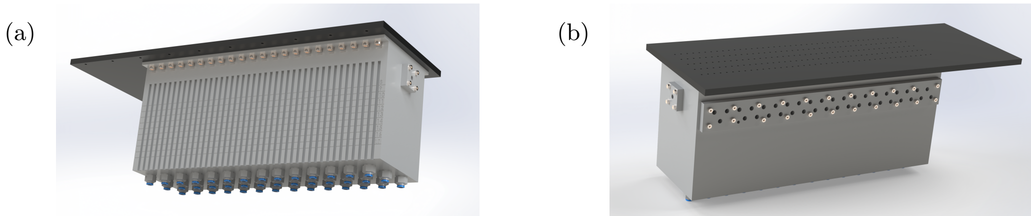

Figure 4.7: Render of the assembly for the configuration 1.

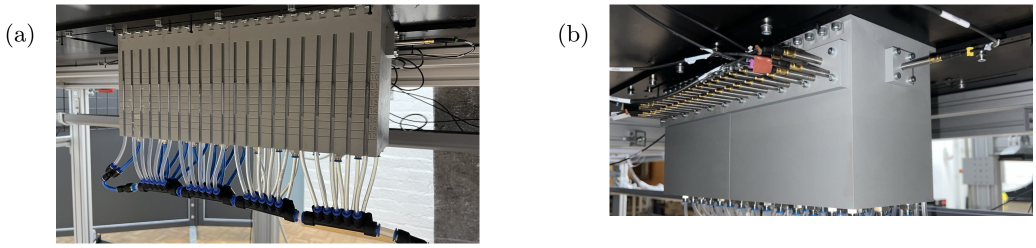

Figure 4.8: (a) Side of the cavities box with the transparent tubes mounted. (b) Side of the cavities box with the microphone installed.

On one side of the boxes, a pattern of transparent pipes was installed alongside a graduated scale, which was useful for ensuring a consistent water level across all cavities. Figure 4.8(a) shows a photo of the experimental setup for configuration 2, highlighting the side where the transparent pipes are installed. On the other sides of the boxes, microphones for measuring the pressure inside the cavities were installed using four separate 3D-printed plates. The most downstream and most upstream microphones were positioned in the central cavities, while the intermediate microphones were placed in one of the outermost rows of resonators along the streamwise direction. The microphone locations were selected based on the flow symmetry hypothesis, assuming identical behavior in all resonators along the spanwise direction. Figure 4.8(b) shows a photo of the experimental setup for configuration 1, highlighting the side where the microphones are installed.

4.4 Measurements Techniques

This section outlines the various measurement techniques employed during the experiments. Sub-Section 4.4.1 provides details on the measurements performed using microphones. Sub-Section 4.4.2 describes the Particle Image Velocimetry technique and its application in this experiment. Lastly, Sub-Section 4.4.3 discusses the hot wire anemometry (HWA) method.

4.4.1 Microphone Measurements

The microphones were embedded in the walls of the cavities' box to measure the fluctuating pressure inside the resonator's cavities during the experiments. Monitoring the pressure inside the cavities was crucial for two main reasons: first, it allowed for the identification of the resonance frequency of the resonators by detecting the most energetic peak in the Fourier transform of the pressure signal. Second, it enabled the synchronization of the pressure signal, within the resonator cavities, with the PIV images, using the Q-switch signal from the laser employed during PIV acquisition.

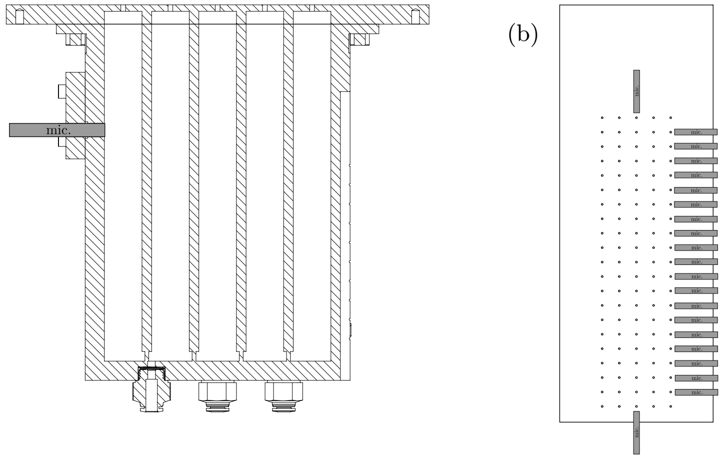

Figure 4.9: Microphones positions in the section view (a) and in the top view (b).

Due to the design strategy, it was not possible to measure the pressure in all the cavities of the setup. Instead, the pressure signal was recorded from the resonators located in the middle of the first and last row of the array, as well as from all the resonators in the rightmost row between the first and last rows. The sketch in Figure 4.9 shows the disposal of the microphones in a section view and in the top view. The employed pressure microphones were the GRAS 40PH-10 CCP, with a nominal sensitivity of 50 mV/Pa and provide an accurate frequency response within ±1.5 decibel over a frequency range of 5 Hz to 50 kHz. Their dynamic range extends from 33 to 135 dB. Using the microphone pressure signals, we evaluated the transfer kernel function, as described in Section 3.4.1. The input pressure signal was taken from the baseline case with a pinhole configuration, following the approach proposed by Dacome et al. (2024). The microphone employed for the pinhole configuration was the GRAS 46BE 1/4-in, with a nominal sensitivity of 3.6 mV/Pa and provide an accurate frequency response within ±1 decibel over a frequency range of 1 Hz to 40 kHz. Their dynamic range extends from 35 to 160 dB.

Table 4.3: Microphones equipments characteristics.

Microphone equipments characteristics		
Microphone	GRAS 46BE 1/4-in	GRAS 40PH-10 CCP
Nominal Sensitivity	3.6 mV/Pa	50 mV/Pa
Frequency Response	±1 decibel	±1.5 decibel
Frequency Range	1 Hz to 40 kHz	5 Hz to 50 kHz
Dynamic Range	35 dB to 160 dB	33 dB to 135 dB

4.4.2 Particle Image Velocimetry

In this section, the measurement technique is the particle image velocimetry, a non-intrusive method used to measure instantaneous velocity fields in fluids such as air or water. This technique relies on illuminating tracer particles, which have a density similar to that of the moving fluid, and capturing their motion with a camera. Once the images are obtained, they are processed using cross-correlation algorithms, which determine the displacement Δs of the tracer particles. By knowing the time interval Δt between the images pairs, the instantaneous velocity field can be calculated as:

$$v_p = \frac{\Delta s}{\Delta t} \tag{4.2}$$

for each point in the region of interest. The PIV acquisition was fundamental to investigate the features of the flow above the resonator's array. In particular a planar two-dimensional two-component (2D2C) PIV was performed in the (x, y) plane, images pairs were acquired with a frame delay of 92 μs with a frequency of 10 Hz, the laser sheet was kept to 1mm thickness using properly set lenses. The illumination was provided by the Quantel Evergreen EVG00200 Nd:YAG laser (maximum energy per pulse of 200 mJ). To accurately see the flow behavior water-glycol droplets of 1 μm are inserted in the wind tunnel using a SAFEX smoke generator. To increase the images resolution two different cameras were employed during the PIV acquisition, in particular two LaVision Imager sCMOS cameras (2560×2160 px^2 at 10 Hz, and a 6.5 μm pixel size) were used. To achieve the highest resolution of the field of views (FOV) two different Nikon lens have been installed on the cameras. In particular for the smaller FOVs two 200 mm Nikon lens have been used, while for the larger FOVs two 60 mm Nikon lens have been employed. All the information concerning the PIV equipment are summarized in Table 4.6.

Three different fields of view (FOVs) were used: a larger one to capture the global flow behavior above the array, and two smaller FOVs near the resonators' orifices to investigate the flow response in detail. The size of all the FOVs are summarized in Table 4.4, both in millimeters and in viscous unit. Each FOV has been captured

Table 4.4: Sizes of the FOVs.

FOV Name	D_x (mm)	D_x^+	D_y (mm)	D_y^+
Small FOV A	35	875	15	375
Small FOV B	42	1050	12.5	312.5
Big FOV	300	7500	120	3000

for the two configurations of resonators array and for the baseline case. The image acquisition, the system synchronization and the PIV processing was performed using the software Davis 10.2 from LaVision. Each FOV is composed by 3 ensemble, in each of them 1000 statistically independent images pairs were acquired to ensure statistical convergence with 3000 image pairs per ensemble. The vector calculation has been performed with a the cross-correlation method, which calculate the instantaneous velocity fields for each image. The size of the initial interrogation window was 64×64 px^2, with a circular $2 : 1$ window shape and 1 pass, the size of the final

Table 4.5: PIV equipments characteristics.

Laser Sheet	
Laser Type	EVG00200 Nd:YAG
Manufacturer	Quantel Evergreen
Maximum energy	200 mJ
Wavelength	532 nm
Thickness	1 mm
Camera	
Model	LaVision Imager sCMOS
Sensor resolution	$2560 \times 2160\ px^2$
Pixel pitch (size)	$6.5\ \mu m$
A/D conversion	16 bit
Seeding	
Type	atomized water-glycol
Nominal diameter	$1\ \mu m$

(a) (b)

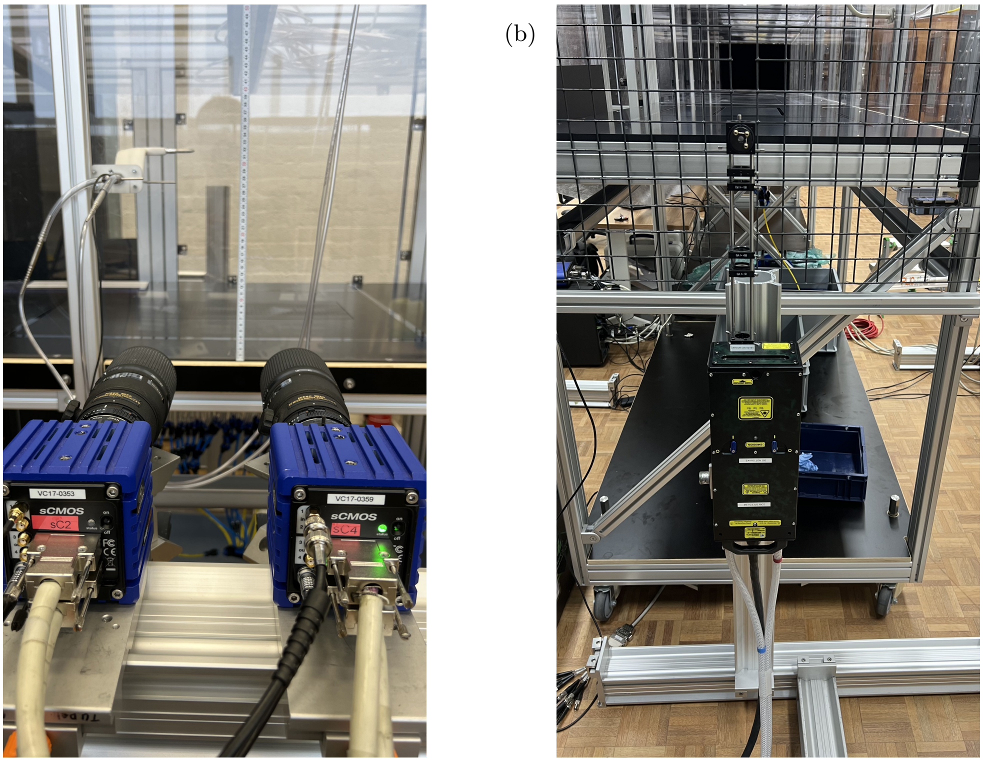

Figure 4.10: Cameras (a) and laser (b) used during the PIV acquisition.

interrogation window was $32 \times 32\ px^2$, with an elliptical window shape, $2:1$ for the smaller FOVs and $4:1$ for the larger FOV, 2 passes were made for the final pass. The overlap was 75% for all the passes. The smaller FOVs were located one downstream the array above the lasts resonators row (Small FOV A), whereas the

Table 4.6: PIV processing characteristics.

Images Processing		
	Small FOV A/B	Big FOV
FOV Size	$35 \times 12.5\ mm^2$	$300 \times 120\ mm^2$
Image resolution	$18\ px/mm$	$18\ px/mm$
Processing technique	Cross-Correlation	Cross-Correlation
Initial Pass Window Size	$64 \times 64\ px^2$	$64 \times 64\ px^2$
Initial Pass Window Shape	$1:1$	$1:1$
Number of Initial Passes	1	1
Final Pass Window Size	$32 \times 32\ px^2$	$32 \times 32\ px^2$
Final Pass Window Shape	$2:1$	$4:1$
Number of Final Passes	2	2

second one was located upstream the array, above the firsts unitrows (Small FOV B). Each FOVs was recorded for both the array configurations and for the baseline case; in Figure 4.11 the dimensions and the positions of the FOVs with respect to the array size are depicted.

(a) (b)

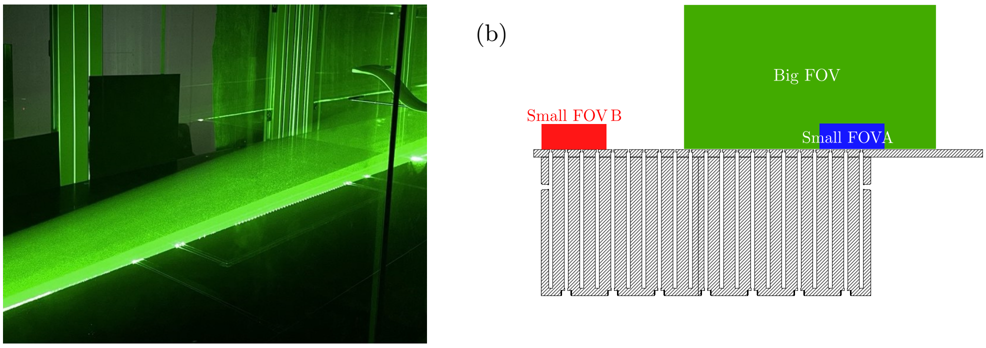

Figure 4.11: (a) Photo during the PIV acquisition. (b) Sketch of the locations of each FOV.

4.4.3 Hot Wire Anemometry

Hot-wire anemometry is a powerful technique used to measure turbulent flows, as it ensures a high-frequency response, good spatial resolution, and provides a continuous signal over time. The working principle of hot-wire anemometry is based on the Joule effect, which enables the determination of the flow velocity by measuring the voltage of a heated metal wire that is cooled by the flow itself. The HWA probe used in our case was capable of measuring only the streamwise component of the velocity. However, it allowed us to record velocity profiles along the wall-normal direction at different locations in the vicinity of the resonator orifices. This can be considered a limitation compared to PIV measurements, which allow for the measurement of both the streamwise and wall-normal components of the velocity field. Nevertheless, due to the high frequency of HWA measurements, spectral analysis can be performed using these data, enabling further investigation into the periodic behavior of the resonators. A Dentec 55P15 miniature-wire boundary layer probe has been used in our measurements, it has a sensing length of $l_w = 1.25$ mm and a length-to-diameter ratio of $l_w/d_w = 250$. The regulation of the probe signal and its response were managed by a TSI IFA-300 bridge.

Table 4.7: HWA equipments characteristics.

HWA equipments characteristics	
Anemometer	IFA 300
Hot Wire Probe	Dentec 55P15
Sensing Length	1.25 mm
Length-to-Diameter Ratio	250
Temperature Range	50°
Traverse	Zaber (three-stages)
Sampling Frequency	51200 Hz

However, hot-wire anemometry is not an absolute measuring instrument, as it responds with a voltage signal when the sensor is cooled by the flow. Therefore, calibration is necessary to use the measuring instrument properly. The calibration process allows the conversion of the sensor's output voltage into the corresponding flow velocity and direction. In our case, 17 different flow velocity values measured using a Pitot-static tube, ranging from 0 m/s to 15 m/s, were used for the calibration process. The conversion from the voltage signal to the velocity signal was carried out using a $4th$-order polynomial interpolation, implemented in a custom LabVIEW program. Due to variations in environmental conditions throughout the experiments, the calibration process was periodically repeated during data acquisition.

Before the data acquisition, an essential step was positioning the probe as close as possible to the wall. To achieve this, the PIV acquisition cameras, calibrated using the calibration target, were utilized to measure the distance between the probe and the wall. Figure 4.12 shows an image of the probe near the wall, where Δy is 2 times the distance of the probe from the wall. The probe's position relative to the wall was determined by dividing by two the measured distance between the probe and its reflection on the wall.

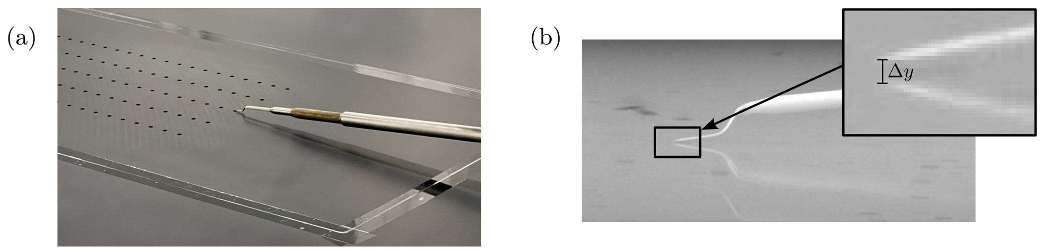

Figure 4.12: (a) Hot-wire probe above the array. (b) Position of the hot wire probe with respect to the wall.

For each velocity profile, 20 logarithmically spaced points in the range $y^+ \in (5, 630)$

were acquired. Subsequently, in the hot wire post-processing data, the wall locations were shifted accordingly, to the wall distance measured with the previously described technique. Each point within a velocity profile consists of a voltage signal recorded for 100 s with a sampling frequency of 51200 Hz. The velocity profiles were acquired at different positions in the (x, z) plane of the resonator arrays. Specifically, four velocity profiles were recorded in the symmetry plane of the resonators' array at three different streamwise positions downstream of the last resonator: $x^+ = 120, 250, 500, 1000$. In Figure 4.13 a sketch of the HWA velocity profile positions in the (x, z) plane is shown. Finally, in order to quantify the effects of the array with respect to a reference case, two different profiles were acquired for the baseline case, i.e. a normal flat plate. The first profile with 20 points has been disposed as in the velocity profiles previously described, while for the second one 40 different points have been acquired, logarithmically spaced in the range $y^+ \in (5, 4500)$.

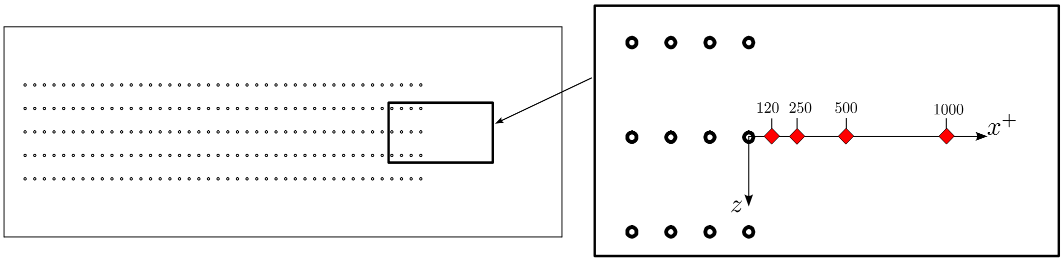

Figure 4.13: Position of the HW velocity profiles in the streamwise direction (red diamonds).

Chapter 5

Results

In this chapter the results from the experiments are shown. In the first Section 5.1 the Helmholtz resonators' excitation by turbulent boundary layer flow is analyzed, using the microphones embedded in the resonators cavities. In the next Sections 5.2, 5.3 the mean streamwise velocity profiles and the streamwise Reynolds stress profiles respectively, in the wake of the arrays are observed using the data from the hot-wire anemometry. From the hot-wire the data, is also performed a spectral analysis on the energy content of the streamwise velocity fluctuations, in Section 5.4. Subsequently in Section 5.5, the images from the PIV are used to plot the mean fields of the flow in the vicinity of the orifices of the resonators. Meanwhile in Section 5.6 the PIV images are plotted phase-averaged on the microphone signal within the resonators' cavities to see periodicity behavior of the flow above the array. Lastly in Section 5.8, the skin friction coefficients are computed in the wake of the arrays for different streamwise positions adopting different methods.

5.1 Helmholtz Resonators' Excitation by Turbulent Boundary Layer Flow

This section presents the measurements obtained from microphones placed inside the resonator cavities, focusing on analyzing the resonator's response to turbulent flow excitation. Due to the limited number of input pins on the data acquisition module, only ten microphone signals were recorded during the experiments.

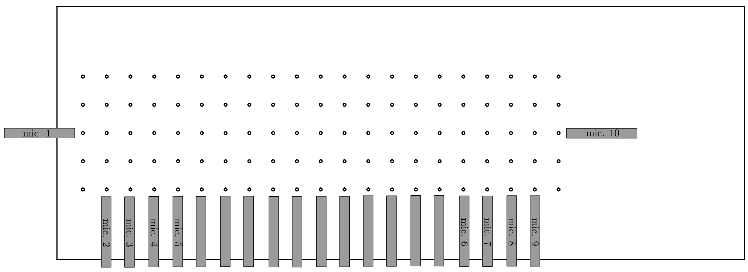

Figure 5.1: Positions of the ten recorded microphone signals in the array. This sketch illustrates configuration 2, the same layout is applied for configuration 1.

Specifically, the first five and the last five microphones along the streamwise direction were considered, as shown in Figure 5.1. From the recorded signals has been possible to compute the resonators' transfer kernel:

$$|H_{HR}| = \sqrt{\frac{\phi_{p_c p_c}(f)}{\phi_{p_i p_i}(f)}} \tag{5.1}$$

where p_c is the pressure measured inside the resonators' cavities and p_i is the pressure in the inlet of the resonators' orifices. The inlet pressure signal was recorded during the baseline flow measurements with the wall-embedded microphone in a pinhole configuration. Secondly the power spectral density (PSD) of the transfer kernel for each signal was computed using Welch's method to identify the dominant peak frequency for each microphone. To reduce noise, ensemble averaging was performed. The signal was segmented into portions using $N = 2^{14}$ samples, with a Hanning window applied to each segment and a 50% overlap between consecutive windows. In Figure 5.2, the gain of the PSD for the transfer kernels are presented, with the dominant peaks highlighted by solid red circles. It is evident that these peaks occur at the same frequency in each cavity along the streamwise direction, aligning with the Helmholtz resonance frequency established during the design phase, $f_0^+ = 0.04$.

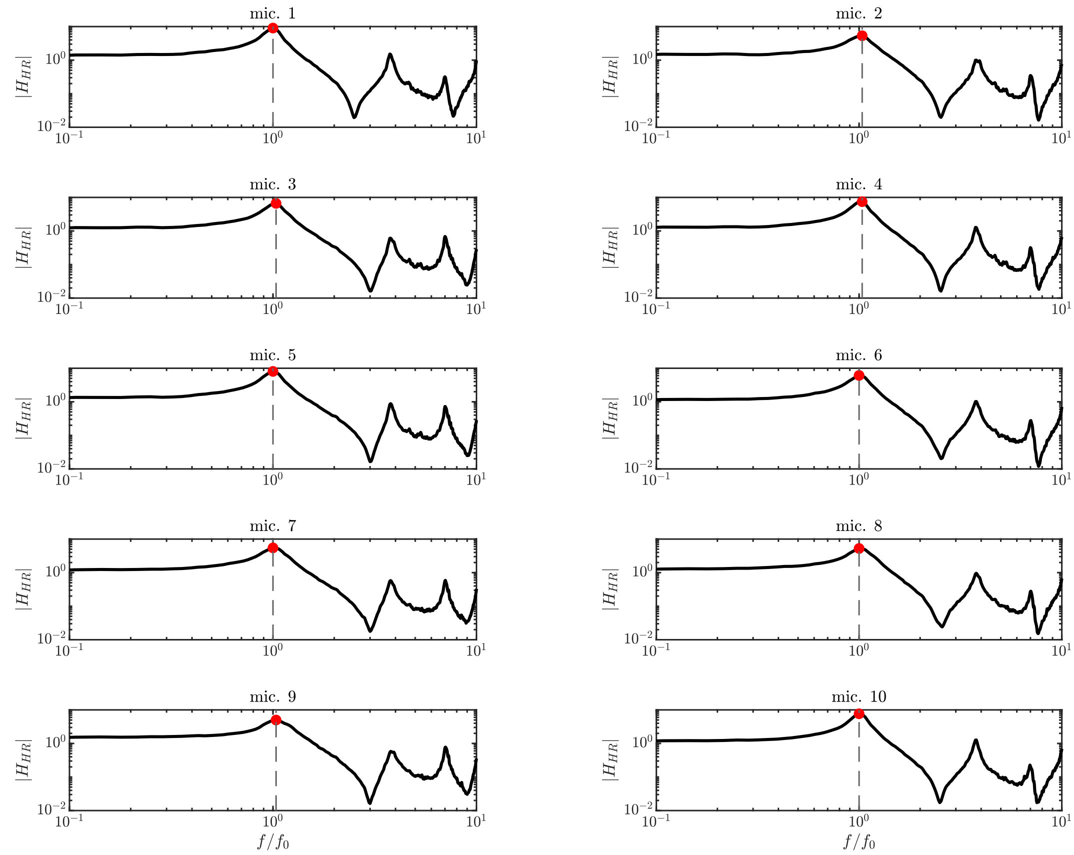

Figure 5.2: Gain response of the transfer kernel for each of the 10 recorded microphone signals. The dominant frequency peaks are marked with solid red circles. The vertical dashed lines correspond to $f/f_0 = 1$.

The plots in Figure 5.2 correspond to the microphone signals recorded under configuration 2. Throughout all the experiments, the resonators' response was monitored; however, for practicality, only these results are presented.

5.2 Mean Streamwise Velocity Profiles

In this Section the flow behavior in the wake of the arrays is investigated employing hot-wire anemometry, previously described in Section 4.4.3. In Figures 5.3, 5.4 the velocity profiles along different streamwise positions in the wake of the array are displayed for the configuration 1. In the plots also the profile from the baseline case and the profile from DNS data of Lee and Moser (2015) are shown as reference profiles. Furthermore, all velocity profiles are normalized using viscous dimensions computed from the baseline profile as. Additionally, the profiles' positions relative to the wall have been further adjusted by minimizing the error between each profile and the DNS profile across the entire profile.

As result from Figure 5.3 discrepancy between the velocity profiles embedding the configuration 1 and the baseline profile can be noted. In particular in the zoom on the log-region, in Figure 5.3(b), lower values of mean streamwise velocities are found compared to the baseline for the velocity profiles taken at $x^+ = 120, 250, 500, 1000$ for all the results form the HW measurements, the reference frame is defined with its origin in the center of the last resonator in the array). It can also be observed that the previously described effect is less pronounced in the velocity profile measured farther from the wall at $x^+ = 1000$ compared to the profile recorded closer to the last spanwise row of resonators. This could be due to the recovery of the flow from the effects of the array, when measuring far from the last resonators.

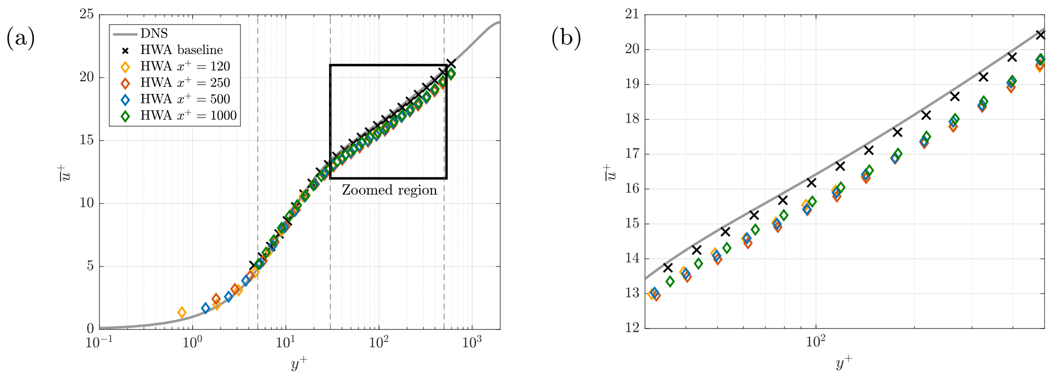

Figure 5.3: (a) Mean streamwise velocity profiles at different streamwise locations for the configuration 1. The vertical dashed lines are the boundaries between the different regions of a turbulent boundary layer profile, $y^+ = [15, 30, 500]$, described in Section 2.3.1. (b) Zoom in the log region of the previous plot. For all profiles, the values have been normalized using u_τ from the baseline case.

In Figure 5.4, the velocity profiles in the wake of the array are presented for configuration 2, measured at the same streamwise locations as in the previous configuration. In this case, it is evident that the effect of the array on the mean streamwise velocity profiles is minimal. The velocity profiles in the wake of the array for configuration 2 substantially follow the one from the baseline case. This suggests that the impact on the mean streamwise velocity profiles in the wake of the array is more significant when the spacing between the spanwise rows of resonators corresponds to that used in configuration 1 ($\Delta x_1^+ = 250$) rather than the larger spacing employed in configuration 2 ($\Delta x_2^+ = 500$).

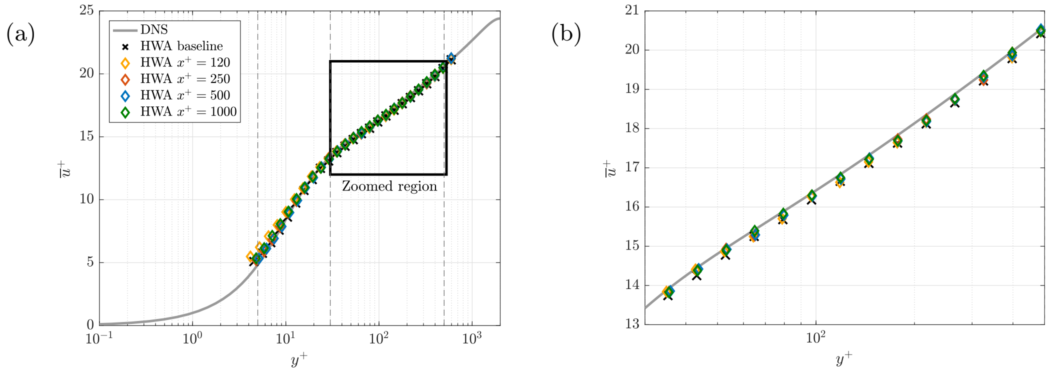

Figure 5.4: (a) Mean streamwise velocity profiles at different streamwise locations for the configuration 2. The vertical dashed lines are the boundaries between the different regions of a turbulent boundary layer profile, $y^+ = [15, 30, 500]$, described in Section 2.3.1. (b) Zoom in the log region of the previous plot. For all profiles, the values have been normalized using u_τ from the baseline case.

5.3 Streamwise Reynolds Stress Profiles

The hot-wire anemometry technique proves to be highly effective in estimating streamwise velocity fluctuations across different wall-normal positions. By computing the variance between the instantaneous and mean streamwise velocities at each wall-normal position, it is possible to determine the streamwise Reynolds stress, $\overline{u'u'}^+$. This quantity serves as an indicator of the turbulence intensity in the streamwise direction. In Figure 5.5 and 5.6 the streamwise Reynolds stress is shown for configuration 1 and for configuration 2, respectively. As depicted for the mean streamwise velocity profiles in Section 5.2, also in this case the profiles are compared with the one from the baseline case and the one from the DNS data of Lee and Moser (2015).

Considering the $\overline{u'u'}^+$ profiles in the wake of the configuration 1, shown in Figure 5.5, significant discrepancies can be observed along all the profiles, with respect to the baseline case. For all the four streamwise locations, $x^+ = [120, 250, 500, 1000]$, an increase of streamwise velocity fluctuations is registered closer to the wall, where $y^+ < 100$, while a decrease of the streamwise Reynolds stress is marked farther from the wall, for wall normal positions higher than $y^+ = 100$. Another observation can be made concerning the position of the $\overline{u'u'}^+$ profile's peak which is shifted closer to the wall when the array is embedded in comparison of the baseline case.

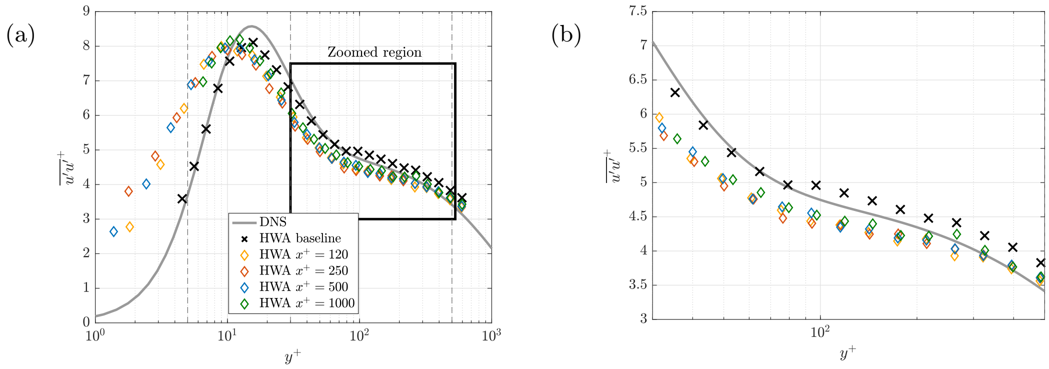

Figure 5.5: (a) Streamwise Reynold stress profiles at different streamwise locations for the configuration 1. The vertical dashed lines are the boundaries between the different regions of a turbulent boundary layer profile, $y^+ = [15, 30, 500]$. (b) Zoom in the log region of the previous plot. For all profiles, the values have been normalized using u_τ from the baseline case.

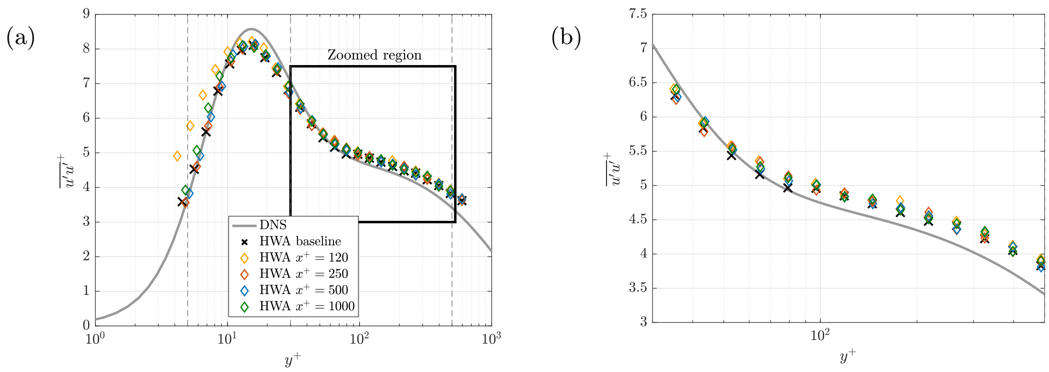

Figure 5.6: (a) Streamwise Reynold stress profiles at different streamwise locations for the configuration 2. The vertical dashed lines are the boundaries between the different regions of a turbulent boundary layer profile, $y^+ = [15, 30, 500]$. (b) Zoom in the log region of the previous plot. For all profiles, the values have been normalized using u_τ from the baseline case.

In the meantime, we can observe the effect of configuration 2 on the streamwise Reynolds stress profile in the wake of the array, as shown in Figure 5.6. With this array configuration, there are minimal discrepancies between $\overline{u'u'}^+$ and the baseline profile. In particular, far from the wall, as illustrated in Figure 5.6(b), the trends of the profiles at different streamwise locations remain highly similar. However, small discrepancies can be observed closer to the wall, for y^+ positions below approximately $y^+ \approx 10$, and only at streamwise locations near the last spanwise row of resonators, $x^+ = 120$. This indicates the relatively minor effect of configuration 2, which features a lower concentration of resonators. The influence of this configuration becomes quite evident only very close the end of the array, whereas in configuration 1, the effect was noticeable up to $1000l_\nu$ from the array's end.

5.4 Spectral Energy of Streamwise Velocity Fluctuations

The hot-wire anemometry data prove to be highly valuable for evaluating the energy distribution of streamwise velocity fluctuations across different scales. This is made possible by the high sampling frequency of the measurements, which enables data to be recorded over a broad frequency range, up to half of the sampling frequency, according to the Nyquist theorem. Capturing data across this wide frequency range allows for a detailed analysis of energy distribution among different scales within the turbulent boundary layer. The mathematical tool used to quantify the amount of energy per scale is the spectral energy density, introduced in Section 2.5.

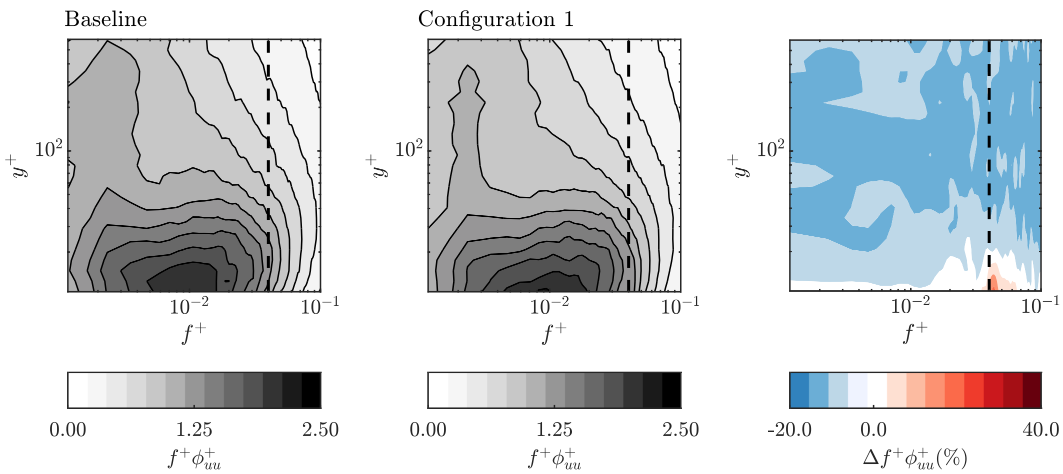

Figure 5.7: Percentage difference of the pre-multiplied energy spectrogram at $x^+ = 120$ for the configuration 1. The vertical dashed line is the resonance frequency $f_0^+ = 0.04$.

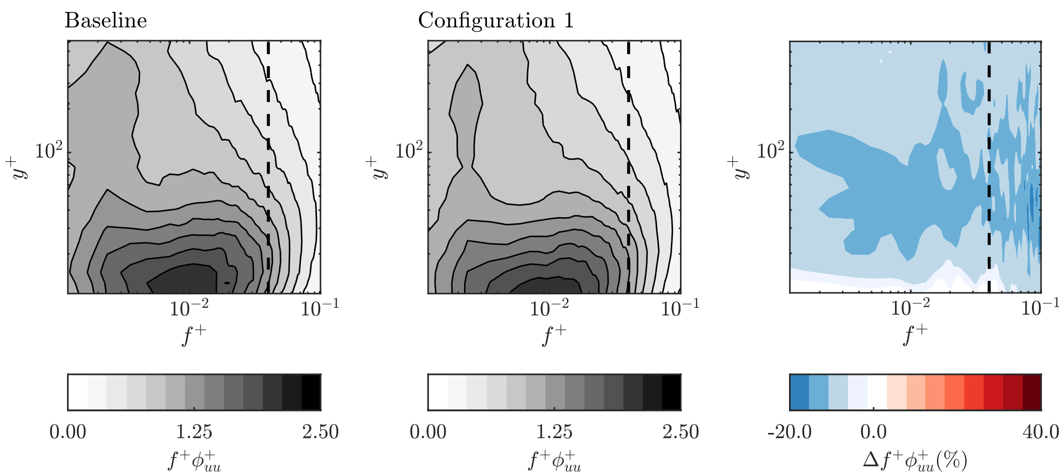

Figure 5.8: Percentage difference of the pre-multiplied energy spectrogram at $x^+ = 250$ for the configuration 1. The vertical dashed line is the resonance frequency $f_0^+ = 0.04$.

In Figures 5.7 - 5.12 the contour plots of the premultiplied spectrograms $f^+\phi^+_{uu}$ are

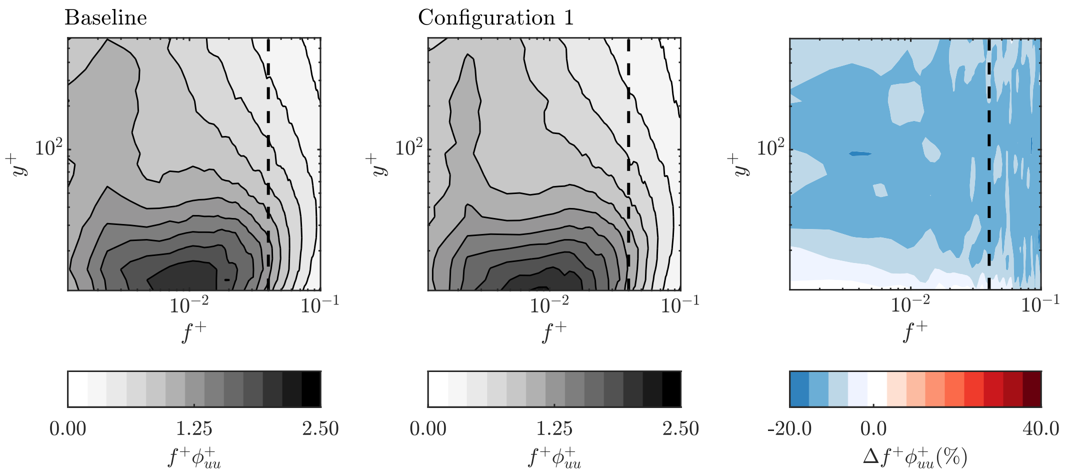

Figure 5.9: Percentage difference of the pre-multiplied energy spectrogram at $x^+ = 500$ for the configuration 1. The vertical dashed line is the resonance frequency $f_0^+ = 0.04$.

shown at different wall-normal positions, emphasizing the dependence of energy distribution from y^+ and f^+. Each figure presents the spectrogram for the baseline case, followed by the configuration-embedded case, and finally the percentage difference between the two, highlighting variations in energy across different scales. Each figure presents the premultiplied spectrogram at a different streamwise locations, specifically at: $x^+ = [120, 250, 500]$. The last coordinate, $x^+ = 1000$, has been excluded from this section due to the negligible effects observed.

Starting from the spectrogram closer to the wall embedding configuration 1, in Figure 5.7, a 15% to 20% amplification of energy is present around and above the resonance frequency $f_0^+ = 0.04$ of the Helmholtz resonators. This energy amplification reaches up to $y^+ \approx 15$ and seems to vanish as soon as a farther streamwise position is taken in account, as displayed in Figures 5.8 and 5.9. At the same time, there is clear evidence 5% to 20% of energy attenuation across the rest of the spectrogram, affecting frequencies both above and below the resonance frequency and extending across all wall-normal positions. Additionally, the energy attenuation effect appears to weaken as the spectrogram is computed farther from the last resonator. This trend is evident in Figures 5.8 and 5.9, where the percentage difference plots generally indicate a lower level of energy attenuation.

Examining the spectrogram closest to the end of the array for configuration 2, shown in Figure 5.10, a clear energy amplification is observed around and above the resonance frequency, with a higher percentage, $(20\% - 30\%)$, compared to configuration 1 and reaches a slightly higher wall-normal position $y^+ \approx 30$. The energy amplification effect is still evident only for $x^+ = 120$ and clearly disappears for higher streamwise positions. At the same time, an overall energy attenuation is evident across the rest of the spectrogram, though its intensity is lower, in the order of 2%, than the energy attenuation observed with configuration 1.

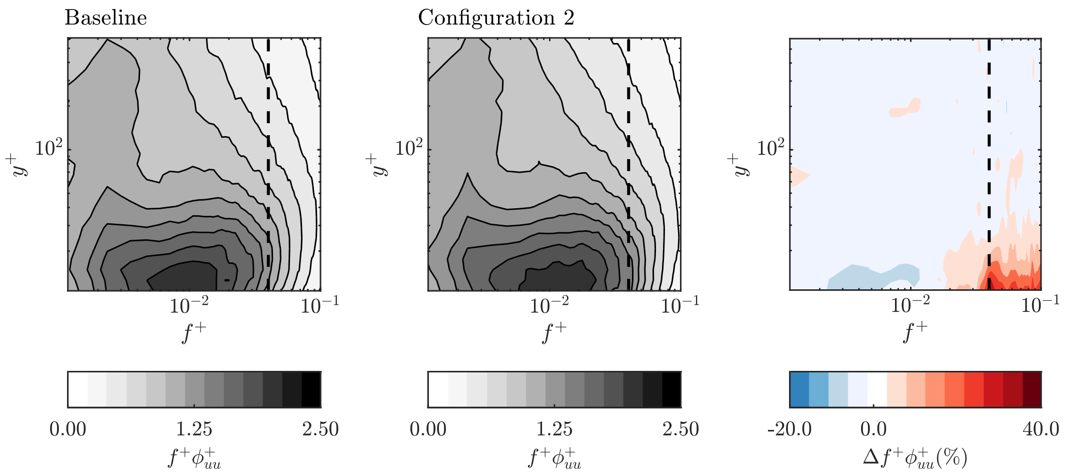

Figure 5.10: Percentage difference of the pre-multiplied energy spectrogram at $x^+ = 120$ for the configuration 2. The vertical dashed line is the resonance frequency $f_0^+ = 0.04$.

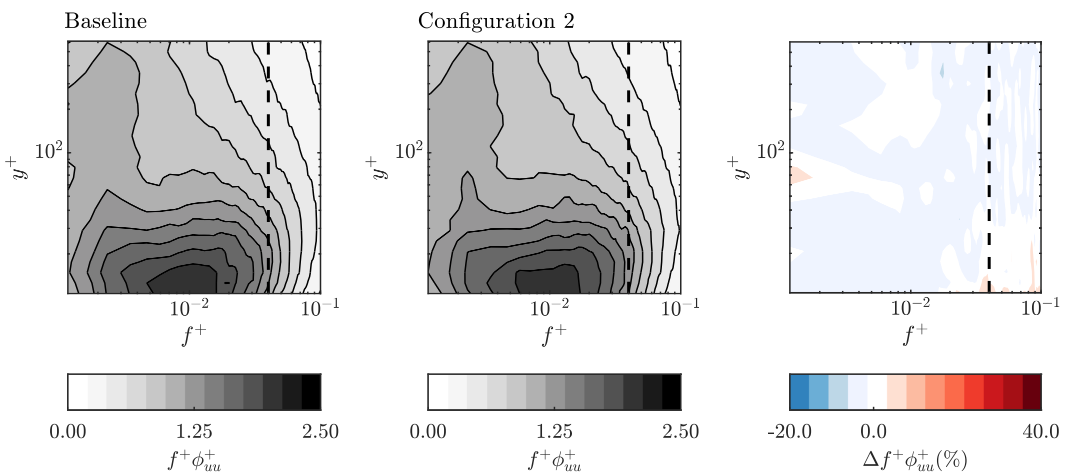

Figure 5.11: Percentage difference of the pre-multiplied energy spectrogram at $x^+ = 250$ for the configuration 2. The vertical dashed line is the resonance frequency $f_0^+ = 0.04$.

We can summarize that, at the examined streamwise positions, configuration 1 leads to an overall higher energy attenuation compared to configuration 2. In contrast, configuration 2 results in greater energy amplification near and above the resonance frequency. This behavior could be attributed to the different u_τ values present in the wake of the different configurations. This parameter is crucial, as all quantities within a turbulent boundary layer scale with it. Consequently, when comparing absolute energy values, as done in the spectral analysis, the percentage difference depends on the variation of u_τ between the two configurations. Specifically, the results here follow the trend of u_τ decreasing, indicating a reduction in energy due to the modified wall shear stress downstream of the array.

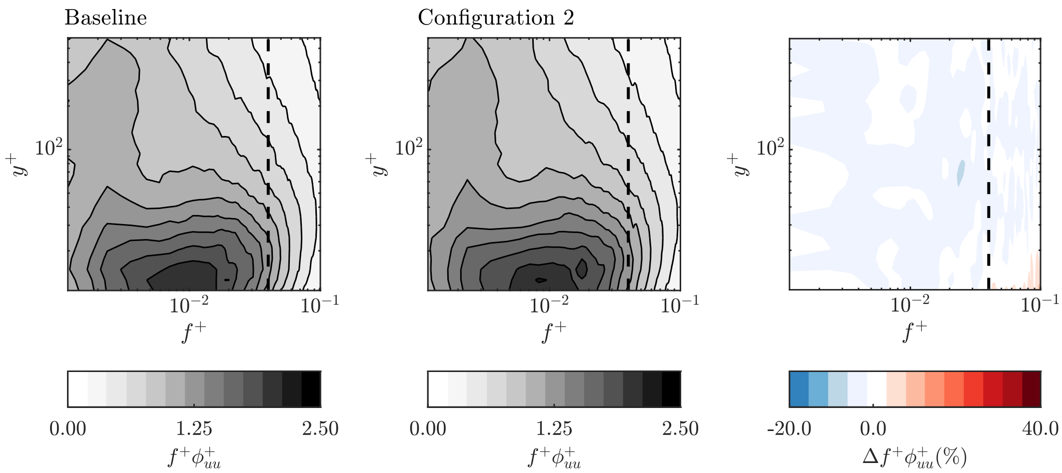

Figure 5.12: Percentage difference of the pre-multiplied energy spectrogram at $x^+ = 500$ for the configuration 2. The vertical dashed line is the resonance frequency $f_0^+ = 0.04$.

Finally, one last observation concerns the lower percentage values observed in the previous spectrograms compared to those reported in Dacome et al. (2024) when testing a single resonator configuration using the HWA technique, as done in this study. This discrepancy may be attributed to differences in the experimental facilities. In particular, the influence of background acoustics on the response of the HR has not been examined in this work. Future studies may explore whether the resonators' response to the turbulent boundary layer is affected by varying noise levels in the wind tunnel.

5.5 Mean Flow Measurements

The hot-wire anemometry measurements provided insights into the flow characteristics solely in terms of streamwise velocity due to the inherent limitations of the measurement technique, as discussed in Section 4.4.3. In contrast, particle image velocimetry allows for the evaluation of both velocity components in the streamwise plane. This section presents an analysis of the mean flow field characteristics derived from the PIV images, focusing on the zoomed fields of view upstream (Small FOV B) and downstream (Small FOV A) of the array. The images captured using the larger FOV (Big FOV) were discarded, as they did not reveal any significant results, probably due to lack of resolution. For each FOV, four different mean fields have been plotted: the streamwise mean velocity field, the streamwise Reynolds stress, the shear Reynolds stress, and the wall-normal Reynolds stress. For all the results form the PIV measurements, the reference frame is defined with its origin in the center of the first resonator in the field of view plotted.

Focusing on the case where images were taken in the downstream FOV, as shown in Figure 5.13, a slight difference in mean streamwise velocity near the wall is observed when the array is embedded, attributed to the presence of the resonators. Additionally, a slight overall increase in $\overline{u'u'}^+$ and $\overline{v'v'}^+$ is observed for both embedded configurations (configuration 1 and configuration 2) compared to the baseline. Meanwhile, an increase in shear stress $\overline{u'v'}^+$ is evident only for configuration 1, while configuration 2 does not show any significant increase.

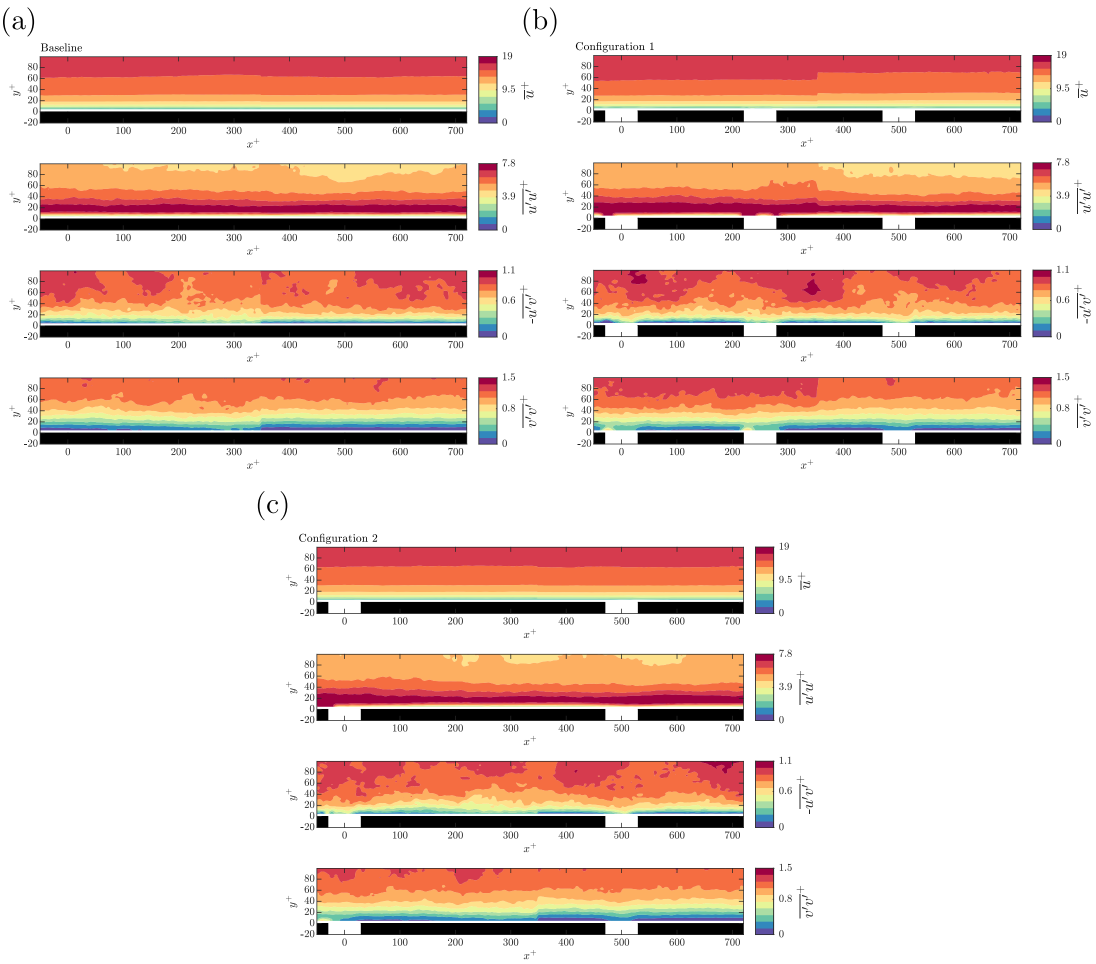

Figure 5.13: Contours of the mean streamwise velocity, streamwise Reynolds stress, shear Reynolds stress, and wall-normal Reynolds stress in the downstream field of view for the baseline case (a), configuration 1 (b), and configuration 2 (c).

The same consideration can be made observing the upstream FOV where the same mean fields have been plotted from the PIV images. In this case only the images from one camera have been employed. Also in this position on the array little difference if streamwise velocity mean fields close to the wall are observed when the array is embedded. A slight increase of $\overline{u'u'}^+$ is noted with both the configurations and a significant increase of $-\overline{u'v'}^+$ is present when the array is embedded, in particular in the vicinity of the first resonator in the array. Lastly, also a relevant increase of wall-normal Reynolds stress $\overline{v'v'}^+$ occurs when the configurations are embedded, in particular close to the first resonator of the array.

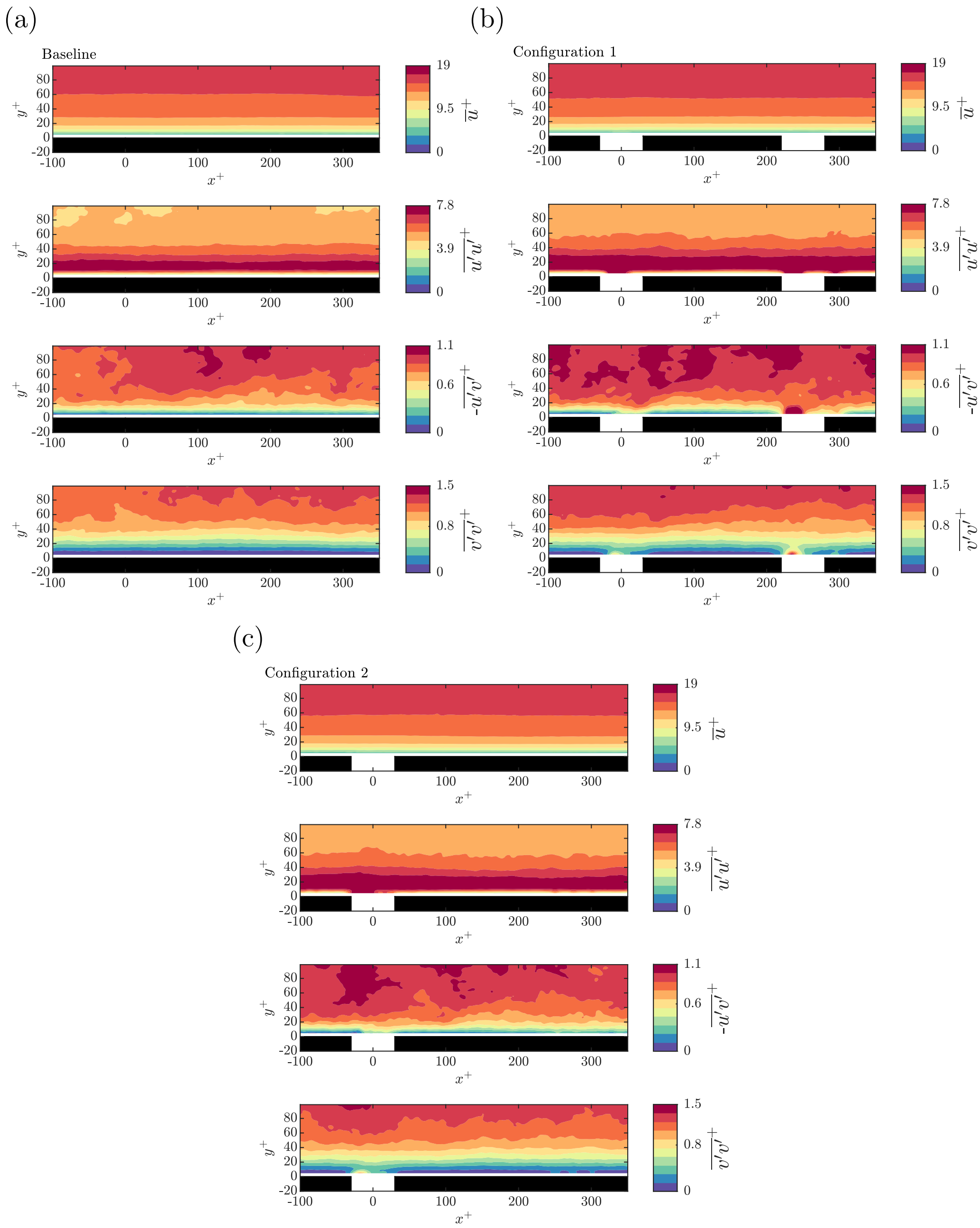

Figure 5.14: Contours of the mean streamwise velocity, streamwise Reynolds stress, shear Reynolds stress, and wall-normal Reynolds stress in the upstream field of view for the baseline case (a), configuration 1 (b), and configuration 2 (c).

5.6 Phase Averaged Flow Fields

In this section, the periodic behavior of the Helmholtz resonators is analyzed through phase averaging the PIV velocity fluctuating fields above the resonators. The synchronized reference signal for phase averaging the PIV fields is obtained from microphones placed within the resonators' cavities. The resonance frequency of each cavity was determined from the gain of the transfer kernel H_{HR}, as described in previous Section 5.1. Subsequently, a band-pass filter was applied to the raw time series signal using a frequency window $f^+ \in [0.6f_0^+, 1.4f_0^+]$ to obtain a smoother signal around the resonance frequency, as shown in Figure 5.15(a). Based on the filtered signal, local maxima in the time series were identified. Each period between two consecutive peaks was then divided into six bins, as illustrated in Figure 5.15(b). Finally, the relative position between two consecutive peaks was computed for each frame and assigned to one of the six bins. To avoid errors during these final stage, any time the period between two consecutive peaks deviated beyond a tolerance threshold from the reference period $1/f_0$, the corresponding frame was discarded. The same process was repeated using a sub-resonance frequency, $f_l^+ = 0.6f_0^+ = 0.024$, with a narrower frequency window, $f^+ \in [0.75f_l^+, 1.25f_l^+]$.

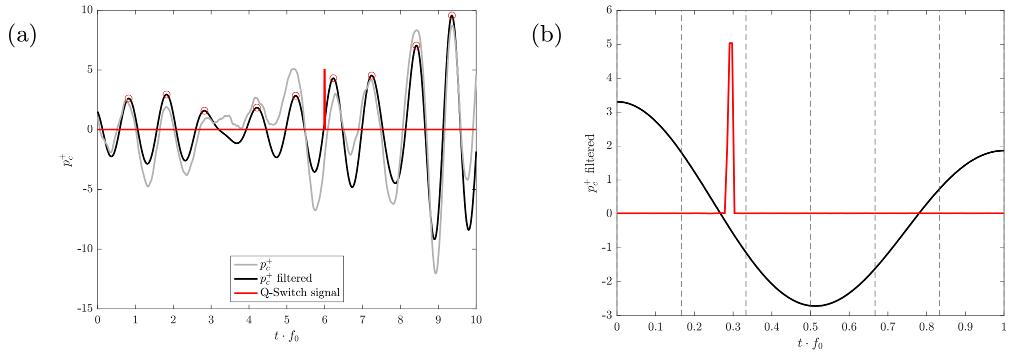

Figure 5.15: (a) Time series of pressure signal inside the resonator's cavity. Ten period are displayed (b) One period divided in the 6 bins used for the phase averaging.

In Figure 5.16, the phase-averaged fields are presented, obtained using the resonance frequency of the first resonator in the array. $\tilde{u'}^+$ and $\tilde{v'}^+$ are the phase-averaged streamwise and wall-normal velocity fluctuations respectively. These fields show the zoomed field of view on the firsts resonator of the array for both the configurations.

On the other hand, in Figures 5.17 the downstream phase-averaged fields for both the configurations are plotted. The red and blue regions in the flow field represent convective perturbations, within the turbulent boundary layer. These structures are characterized by organized patterns of wall-normal velocity fluctuations and their characteristic lengths closely match the wavelength $\lambda_{x,0}^+$ determined from the resonance frequency and the convective velocity in this flow region. Comparing the upstream and downstream FOVs, stronger fluctuations occur close the first resonator compared to the last. This finding aligns with the mean flow observations, where higher Reynolds stress values were observed in the upstream FOVs compared to the downstream ones. Another insight is that the most distinct convective perturba-

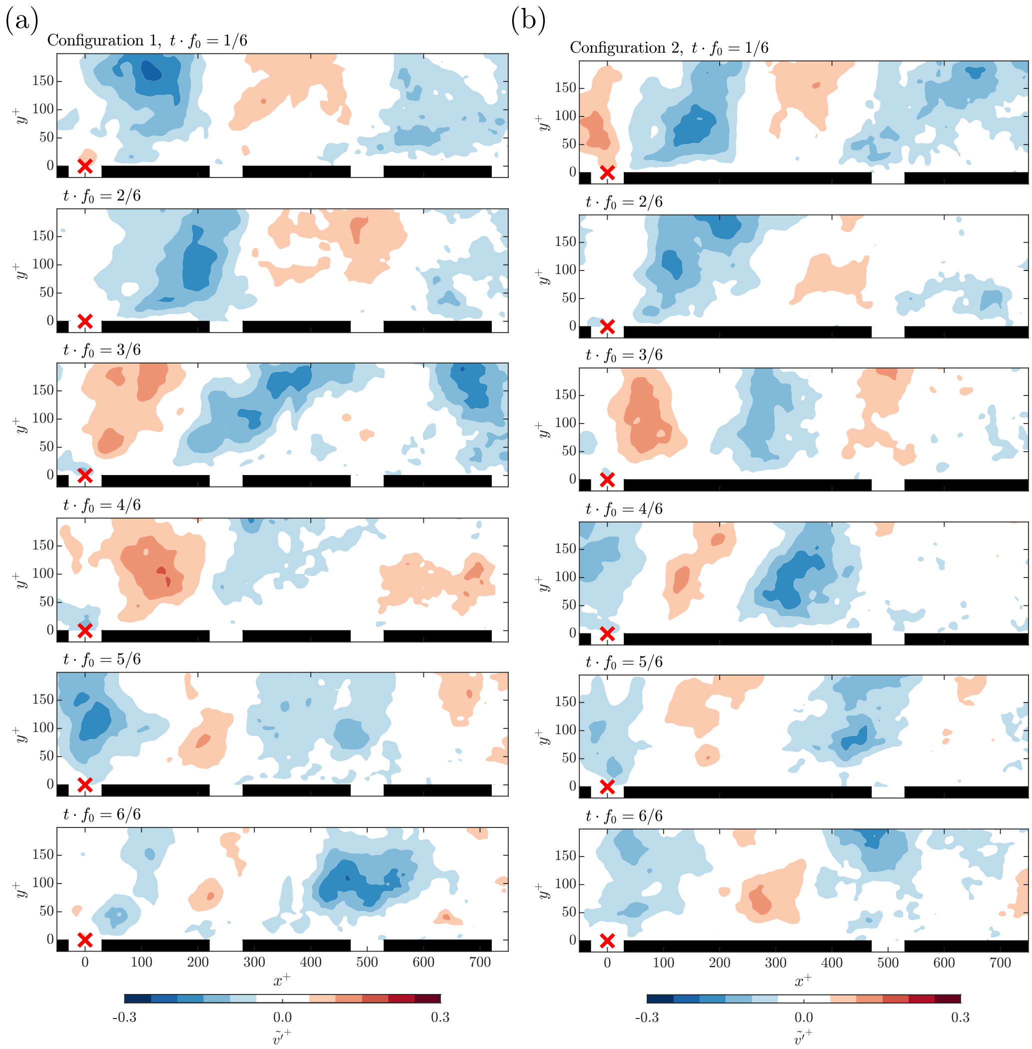

Figure 5.16: Phase-averaged streamwise velocity fluctuations at the resonance frequency $f_0^+ = 0.04$ in the upstream FOV for different cases: (a) configuration 1, and (b) configuration 2 (The red cross marker is the position of the microphone).

tion appear near the resonator's orifice, where the microphone is embedded. As the distance from the microphone increases, the convective turbulent fluctuations become less organized. This occurs because the correlation between the pressure signal recorded inside the resonator's cavity and the velocity fluctuations is stronger in regions closer to the pressure input source. As a result, an increasing phase shift occurs between the pressure signal and velocity fluctuations, leading to inaccuracies in the phase-averaging process.

In Figures 5.18 - 5.21, the PIV fields are phase-averaged using a different frequency to examine the effect of the resonator array in a different scale. Specifically, the phase-averaging was performed using the frequency $f_l^+ = 0.6 \cdot f_0^+ = 0.024$. This value was selected based on observations from the gain plots of H_{HR} in Section 5.1.

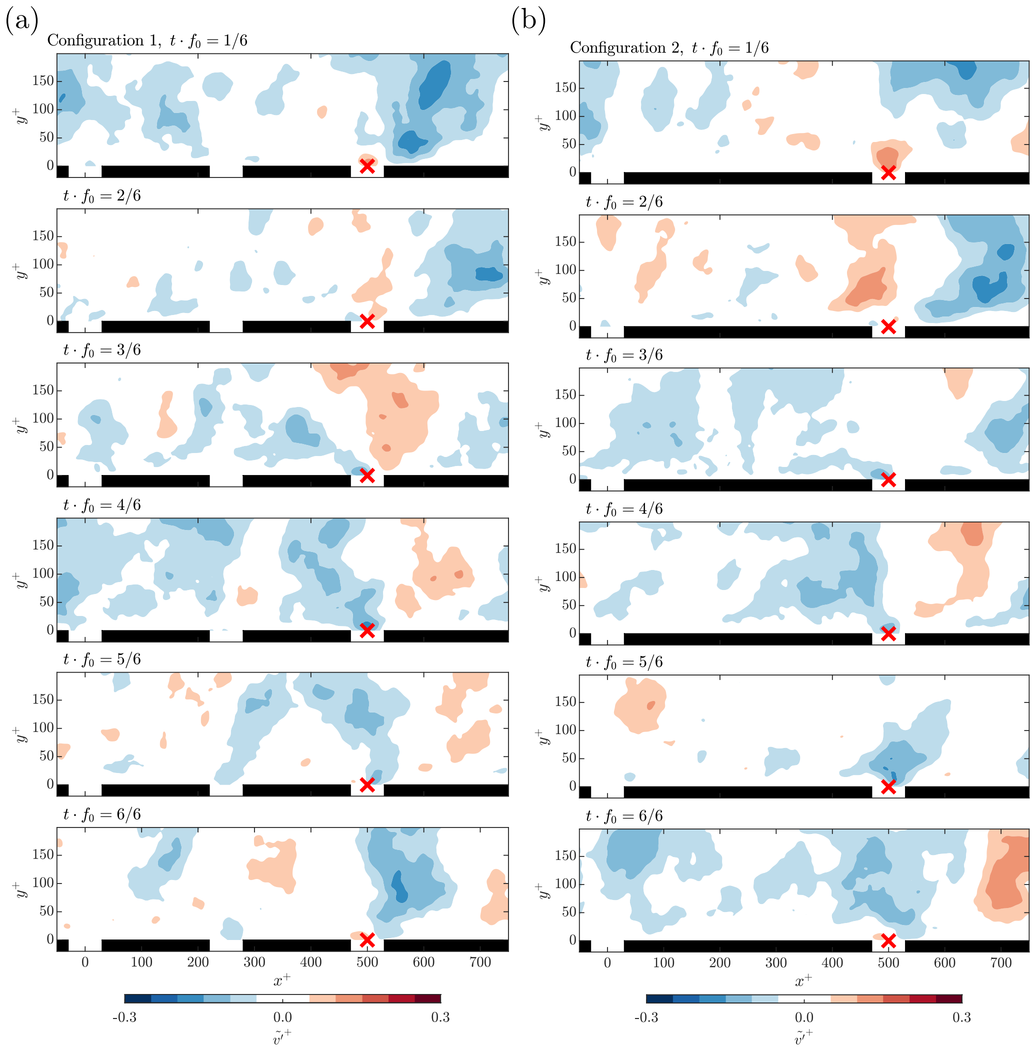

Figure 5.17: Phase-averaged streamwise velocity fluctuations at the resonance frequency $f_0^+ = 0.04$ in the downstream FOV for different cases: (a) configuration 1, and (b) configuration 2 (The red cross marker is the position of the microphone).

Specifically, a value below the resonance frequency was chosen, but one for which the transfer kernel was not equal to 1. Convective turbulent fluctuations near the wall remain present, and the use of a lower phase-averaging frequency results in larger characteristic structure sizes. Additionally, the intensity of wall-normal velocity fluctuations within these structures is higher compared to the fields phase-averaged at the resonance frequency f_0. This happens because the correlation between pressure fluctuations inside the cavity and velocity perturbations depends on the frequency itself. At sub-resonance frequencies, this correlation is stronger than at the resonance frequency, meaning that less information is lost during phase averaging. Consequently, when phase averaging is performed at a sub-resonance frequency, the intensity of the velocity fluctuations appear higher. In the sub-resonance case, it is still observable that the intensity of the velocity fluctuations is stronger in the upstream FOVs compared to the downstream ones. This is consistent with the observations made when

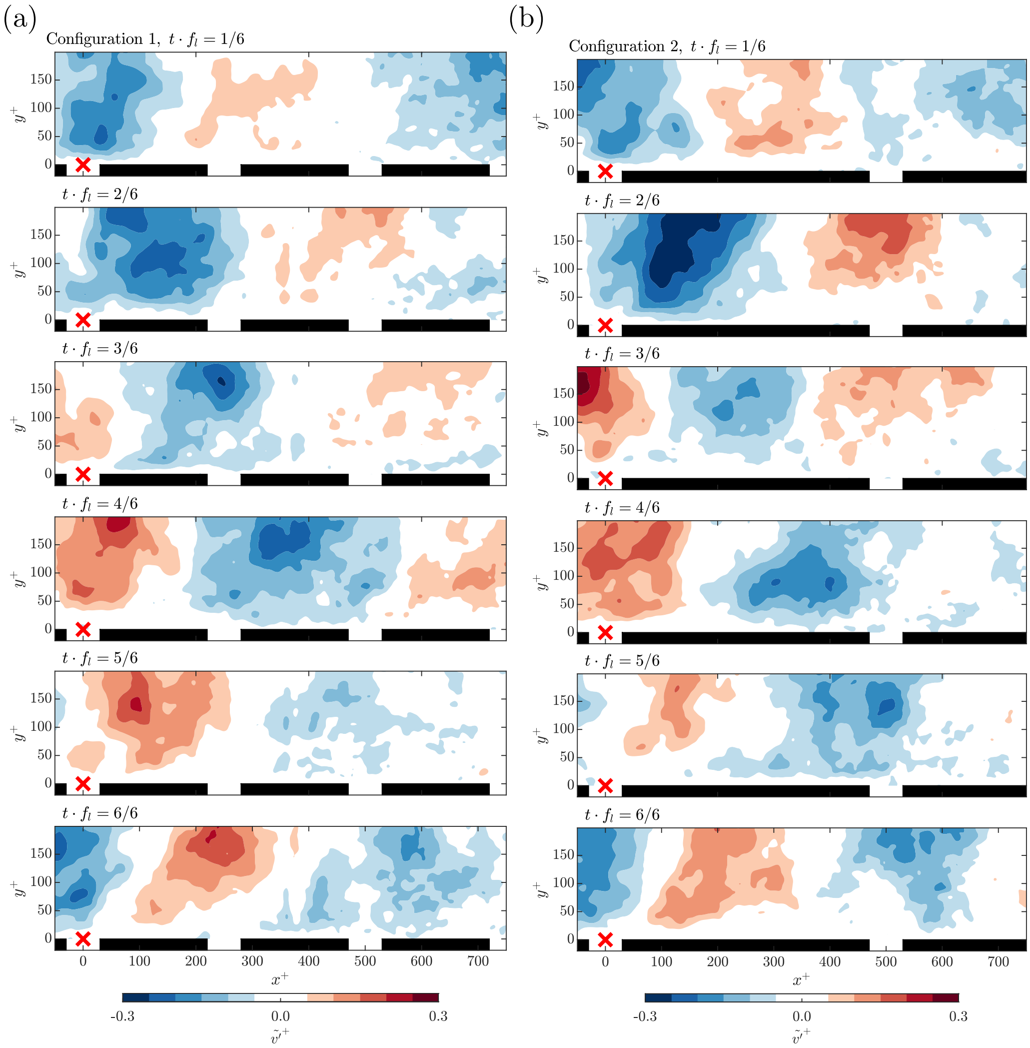

Figure 5.18: Phase-averaged streamwise velocity fluctuations at the sub-resonance frequency $f_l^+ = 0.024$ in the upstream FOV for different cases: (a) configuration 1, and (b) configuration 2 (The red cross marker is the position of the microphone).

phase averaging was performed at the resonance frequency, as well as with the mean flow observations.

The phase-averaged fields of the streamwise velocity fluctuations were also computed using the sub-resonance frequency f_l^+, as shown in Figures 5.20 and 5.21. Even for this velocity component, convective turbulent structures near the wall are present and propagate over the array of resonators. However, the structures appear less distinct when considering streamwise fluctuations. This is likely because the resonators have a greater influence on the wall-normal velocity component than on the streamwise component. As a result, the phase-averaged FOVs appear less organized in this case. However, also in this case stronger streamwise velocity fluctuations are present in the upstream FOVs, in comparison with the downstream FOVs.

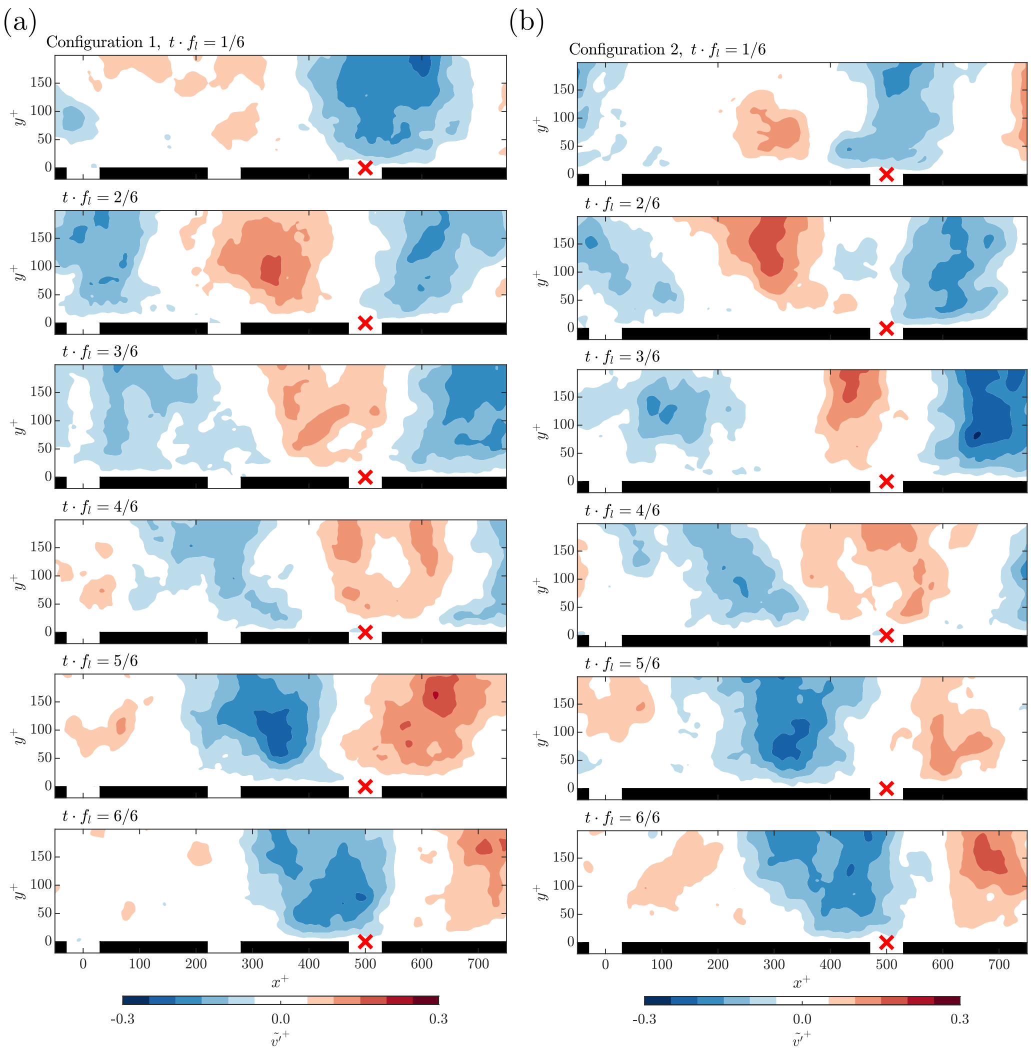

Figure 5.19: Phase-averaged streamwise velocity fluctuations at the sub-resonance frequency $f_l^+ = 0.024$ in the downstream FOV for different cases: (a) configuration 1, and (b) configuration 2 (The red cross marker is the position of the microphone).

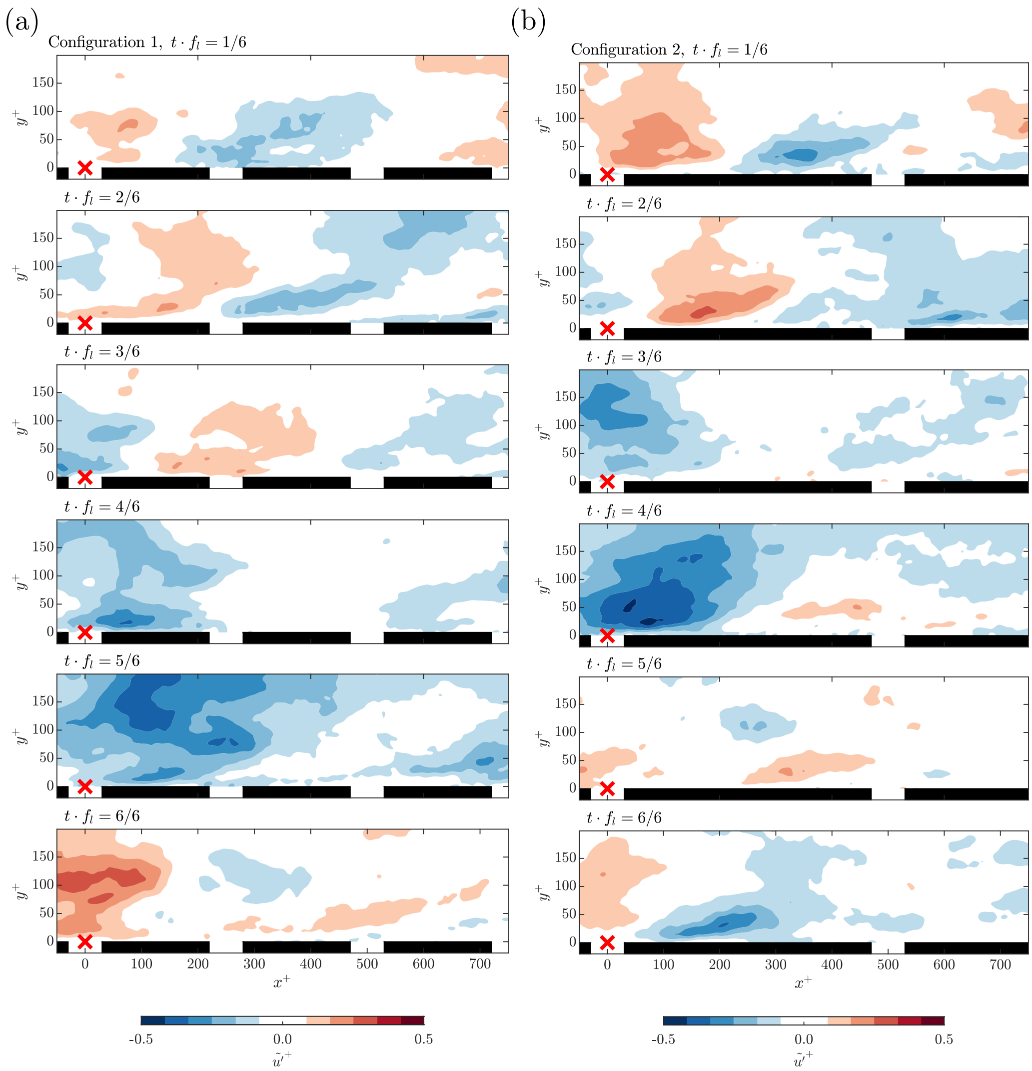

Figure 5.20: Phase-averaged streamwise velocity fluctuations at the sub-resonance frequency $f_l^+ = 0.024$ in the downstream FOV for different cases: (a) configuration 1, and (b) configuration 2 (The red cross marker is the position of the microphone).

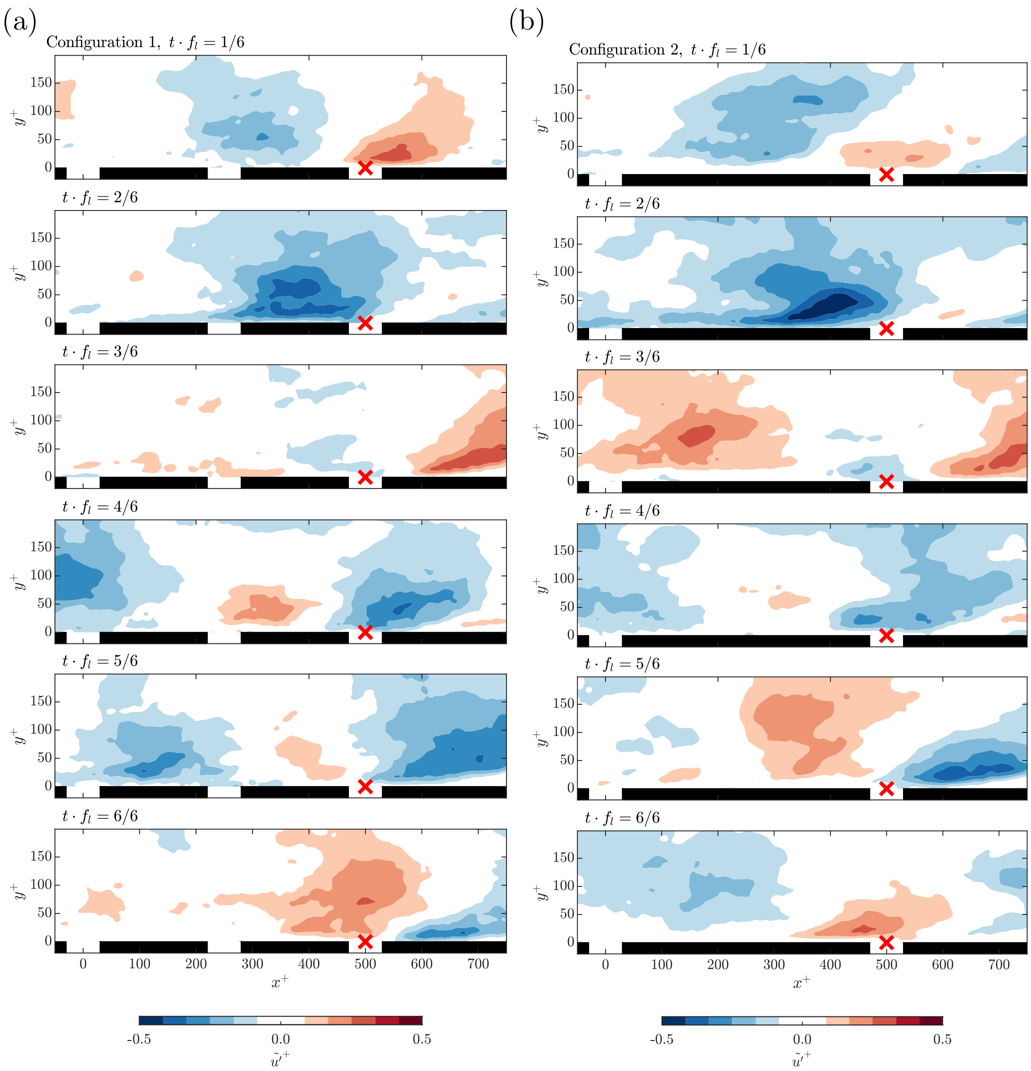

Figure 5.21: Phase-averaged streamwise velocity fluctuations at the sub-resonance frequency $f_l^+ = 0.024$ in the downstream FOV for different cases: (a) configuration 1, and (b) configuration 2 (The red cross marker is the position of the microphone).

5.7 Coupling between pressure and velocity at the neck inlet

This section investigates the relationship between the pressure inside the resonator's cavity and the wall-normal velocity fluctuations above its orifice, thereby revealing the impedance characteristics of the resonators within the array. As described in Section 3.4.2, the pressure variations in the turbulent boundary layer serve as the external force exciting the resonator, while the wall-normal velocity fluctuations correspond to its response. Here, the phase-averaged wall-normal velocity fluctuations are further box-averaged at the resonator's inlet—where the microphone is positioned—over the entire period. The averaging box spans a streamwise length equal to $x \in [-0.3d, 0.3d]$ and a height up to approximately $y^+ \approx 15$. In Figures 5.22 and 5.23 the box-averaged wall normal velocity fluctuations are shown in one period of excitation, respectively in the upstream FOV and in the downstream FOV embedding configuration 1. Figures 5.24 and 5.25 shown the same but embedding configuration 2. The phase averaged cavity pressure $\tilde{p}_c$ is also plotted. Each figure displays both the resonance case at $f_0^+ = 0.04$ and the sub-resonance frequency case at $f_l^+ = 0.024$. The box-averaged wall-normal velocity fluctuations, $\tilde{v'}^+$, shown in the subsequent figures, represent the $v_{resultant}$ fluctuations defined in Section 3.4.2, as the sum of the inherent wall-normal perturbations in the turbulent boundary layer and the fluctuations induced by the resonator. A sinusoidal fit has been applied to these perturbations to clearly reveal their periodic trend.

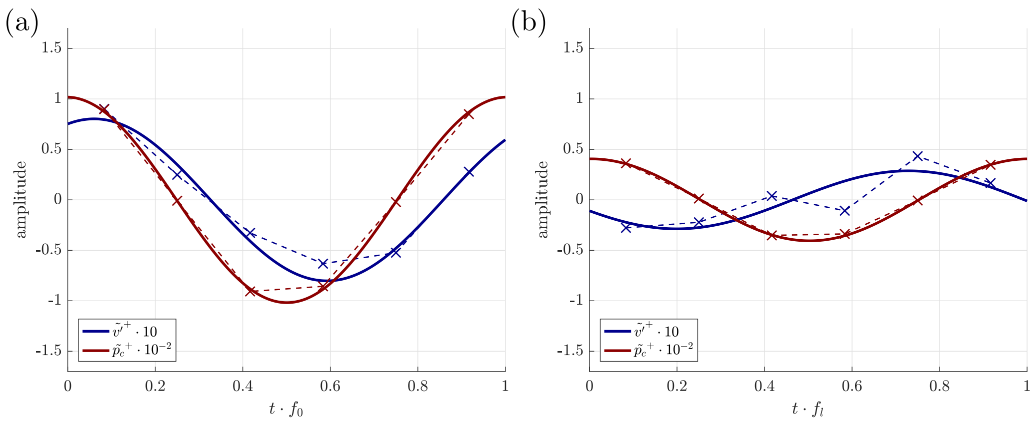

Figure 5.22: Phase-averaged wall-normal velocity fluctuations are box-averaged at the resonator's inlet—where the microphones are located. In this scenario, configuration 1 is considered in the upstream field of view, examining both the resonance frequency (a) and a sub-resonance frequency (b).

Figures 5.22 clearly illustrate that configuration 1 exhibits distinct amplitudes for the box-averaged fluctuating wall-normal velocity at the two frequency values. Specifically, the $\tilde{v'}^+$ fluctuations show a lower amplitude when phase-averaged at the sub-resonance frequency. This observation aligns with the *Resonance-Turbulence Interaction Mechanism* introduced by Hassanein et al. (2024), which postulates that energy is amplified at the resonance frequency and attenuated at sub-resonance frequencies. Although the baseline case is not shown, it is evident that higher fluctuations occur

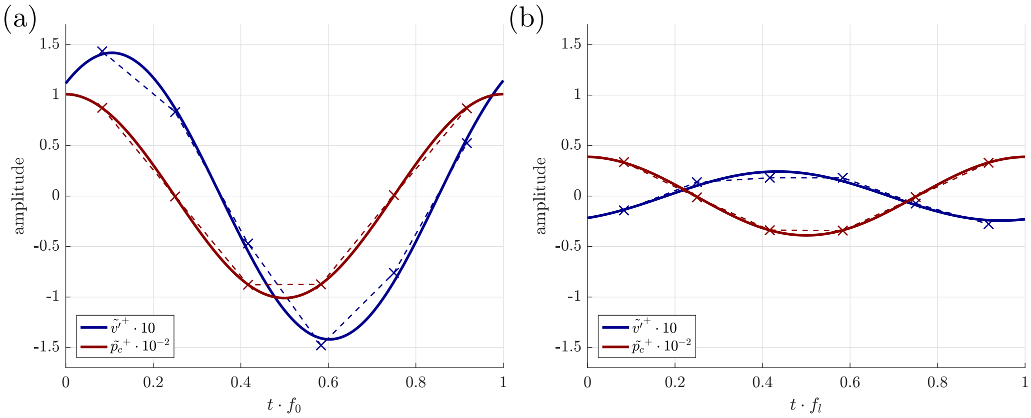

Figure 5.23: Phase-averaged wall-normal velocity fluctuations are box-averaged at the resonator's inlet—where the microphones are located. In this scenario, configuration 1 is considered in the downstream field of view, examining both the resonance frequency (a) and a sub-resonance frequency (b).

at the resonance frequency compared to the sub-resonance frequency.

At the resonance frequency, the fluctuating velocity above the resonator inlet is slightly out-of phase phase with the cavity pressure in both the first resonator of the array (Figures 5.22(a), 5.24(a)) and the last resonator of the array (Figures 5.23(a), 5.25(a)). At the sub-resonance frequency, a phase shift of approximately $-\pi/2$ is observed between the wall-normal velocity fluctuations at the inlet and the cavity pressure in the first resonators of the array, as shown in Figures 5.22(b) and 5.24(b). Conversely, in the last resonators, this phase shift is approximately π, as displayed in Figures 5.23(b) and 5.24. These results suggest that in both configurations, a phase shift of approximately $\pi/2$ occurs between the wall-normal fluctuations and the cavity pressure when comparing the first and last resonators. Therefore, we can conclude that a variation in impedance exists from the first to the last resonator, but only at the sub-resonance frequency.

Observations can also be made regarding the amplitude of the wall-normal fluctuations. Specifically, when the fluctuating velocities are phase-averaged with the resonance frequency, the amplitude is noticeably more intense in the last resonators (Figures 5.23(a) and 5.25(a)) compared to the first (Figures 5.22(a) and 5.24(a)). The amplitude increases by approximately 100% from the first to the last resonator. However, when phase averaging is performed using the sub-resonance frequency, no significant changes in amplitude are observed across the different plots.

Finally, the last remark concerns the plots described in this section. These plots represent the phase-averaged wall-normal velocity fluctuations, box-averaged very close to the resonators' orifice. Consequently, they serve as an indicator of the flow behavior in the vicinity of the orifice inlet, helping to understand the resonator response in terms of wall-normal velocity fluctuations induced by pressure fluctuations

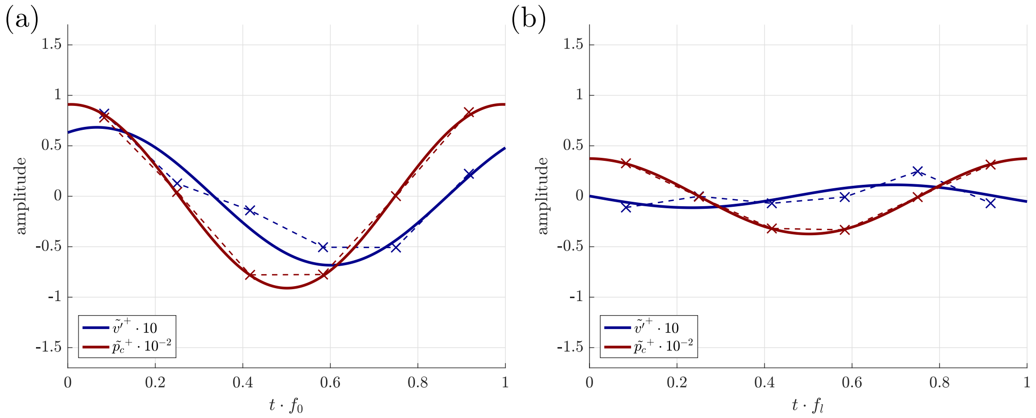

Figure 5.24: Phase-averaged wall-normal velocity fluctuations are box-averaged at the resonator's inlet—where the microphones are located. In this scenario, configuration 2 is considered in the upstream field of view, examining both the resonance frequency (a) and a sub-resonance frequency (b).

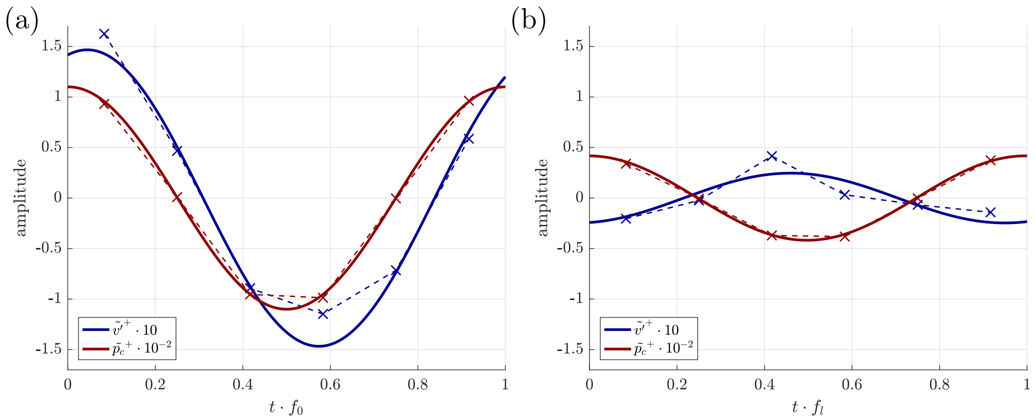

Figure 5.25: Phase-averaged wall-normal velocity fluctuations are box-averaged at the resonator's inlet—where the microphones are located. In this scenario, configuration 2 is considered in the downstream field of view, examining both the resonance frequency (a) and a sub-resonance frequency (b).

within the turbulent boundary layer. However, they do not provide insights into the overall flow behavior above the array. In contrast, the phase-averaged field of view analysis, presented in Section 5.6, aimed to describe the general phase-averaged flow behavior across the entire array.

5.8 Skin Friction Coefficient Downstream the Array

The final results presented in this chapter are derived from the hot-wire data and the PIV fields. In particular starting from the mean streamwise velocity profiles, adopting the method from Clauser (1956), has been possible to compute the skin friction coefficient along different streamwise position for all the tested configurations.

Observing Figure 5.26, which presents the trend of the skin friction coefficient along the streamwise direction, a clear difference emerges between configuration 1 and the baseline, as well as configuration 2. In particular, configuration 2 shows no significant effect on C_f compared to the baseline, a trend that is confirmed by both the HW profiles and the PIV fields. Conversely, when configuration 1 is implemented, a reduction of approximately 6% in the skin friction coefficient is observed in the wake of the array relative to the baseline. This effect gradually diminishes as the distance from the end of the array increases, it shows a possible flow recovery from the effect of the array.

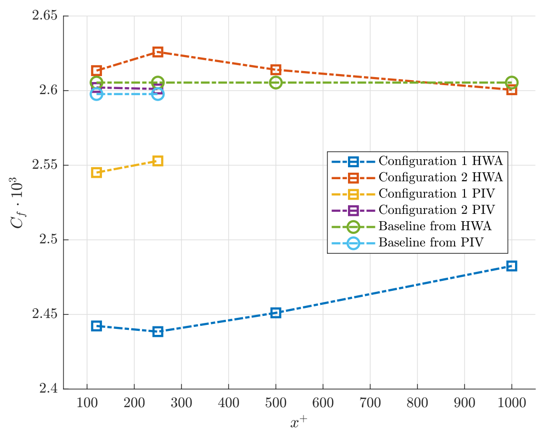

Figure 5.26: Skin friction coefficient downstream the array. In this plot the reference frame the HW measurements is employed.

Chapter 6

Discussion

In this chapter, the results are summarized and discussed. The main findings are highlighted, and comparisons with previous experiments, particularly those involving a single small-scale resonator configuration, are conducted. In the first Section 6.1 the results concerning the sizing, the design and the manufacturing of the arrays are provided. In the next Section 6.2, the focus is on the characteristics of the mean flow observed above the arrays. Section 6.3, on the other hand, discusses the results concerning the frequency-dependent interaction between the resonators and the turbulent boundary layer.

6.1 Size, Design and Manufacture an Array of Small-Scale Helmholtz Resonators

The first challenge of this research was to determine the optimal dimensions for the resonator array and to develop an experimental setup for testing its impact on the flow. The dimensions of the small-scale resonator unit were selected based on the findings of Dacome et al. (2024) and Hassanein et al. (2024), which demonstrated the potential of miniature Helmholtz resonators for manipulating wall Reynolds stress. To establish the most effective streamwise spacing between the spanwise rows of resonators, two different configurations were analyzed. To define the optimal spacing between the rows, it was assumed that each resonator influences a region corresponding to the characteristic wavelength of the most energetic coherent structures in the turbulent boundary layer. Based on this assumption, the spacing between the spanwise rows of resonators was set as a multiple of this wavelength, specifically $\Delta x_1^+ = \lambda_{x,0}^+$ and $\Delta x_2^+ = 2\lambda_{x,0}^+$. The experimental setup was designed with an adjustable volume for the resonators' cavities, allowing control over the Helmholtz resonance frequency. This feature could be beneficial for future experiments exploring different resonance frequency values, employing the same setup.

6.2 Mean Flow Characteristic Above the Helmholtz Resonators' Array

By analyzing the characteristics of the mean flow above the resonators, conclusions can be drawn regarding the differences between the two configurations considered. A clear momentum deficit is observed in the log region of the mean streamwise velocity profile in the wake of the array when configuration 1 is implemented. In contrast, no significant effects are detected when configuration 2 is employed. Similarly, the impact of the array on the streamwise Reynolds stress profile is clearly noticeable only when configuration 1 is implemented. In contrast, for configuration 2, only a slight increase in streamwise Reynolds stress is observed near the wall, and only when the closest position to the end of the array is considered. The same behavior is evident in the final Section 5.8 of the results Chapter, where the skin friction coefficient measured, in the wake of the array, showed minimal variation compared to the baseline case, when configuration 1 was taken in account. In contrast, a significant attenuation of approximately 6% was observed with configuration 1.

Another interesting result, inferred from the analysis of the mean fields, is the variation in Reynolds stress values upstream and downstream of the array, therefore when the first resonator interacts with the turbulent boundary layer and when the array ends. This effect is more evident in the shear Reynolds stress $\overline{u'v'}^+$ and the wall-normal Reynolds stress $\overline{v'v'}^+$ within the buffer layer and the initial part of the log region. This observation suggests that the interaction between the resonators and the turbulent boundary layer evolves along the streamwise direction above the array. However, further conclusions cannot be drawn at this stage, as more studies are needed to fully understand this effect.

The final notable result from the mean flow observations is the variation in skin friction coefficients measured in the wake of different array configurations. This effect is observed only when configuration 1 is embedded, where the spacing between the spanwise rows of resonators is $\Delta x_1^+ = 250$. This suggests that this specific spacing require further investigation, as it has demonstrated better performance in terms of shear-stress manipulation.

6.3 Frequency-Dependent Behavior of the Flow Above the Array of Helmholtz Resonators

The spectral analysis of streamwise velocity fluctuations at different streamwise positions in the wake of the array reveals several interesting findings. At the resonance frequency, an amplification of streamwise velocity fluctuations relative to the baseline case was observed for both configurations, but only at the position closest to the end of the array, $x^+ = 120$. At sub-resonance frequencies, an attenuation of streamwise velocity perturbations was noted, with configuration 1 exhibiting a stronger effect than configuration 2. While no significant increase in attenuation at sub-resonance frequencies was observed, compared to the single resonator case of Hassanein et al. (2024), a reduced amplification at the resonance frequency was detected. Additionally, configuration 2 showed a higher amplification at the resonance frequency than configuration 1, both in terms of its distance from the wall and its percentage difference from the baseline, whereas configuration 1 demonstrated a more favorable effect in reducing amplification. However, as highlighted in Section 5.4, no definitive conclusions can be drawn from these results due to the differences in friction velocity present in the wake of the array when embedding different configurations that alter the absolute energy values in the spectrograms. Additionally, no clear cumulative effect of the Helmholtz resonator array can be observed compared to the single resonator configuration. This is likely due to the different percentage levels, which may be influenced by variations in the noise levels of the facilities used for the experiments.

Considering the results from the phase-averaged field of views from the PIV measurements, one of the objectives was to investigate whether interactions between adjacent Helmholtz resonators emerged. However, no clear evidence of interaction between one resonator and its closest neighbor was observed from the phase-averaged FOV. The interaction between the resonators and the flow was only distinctly visible above the resonator where the microphone was positioned. Consequently, the phase-averaged fields became less defined further from the microphone, making it difficult to identify clear interactions between different resonators. To better understand this phenomenon, a possible solution could be to use signals from multiple microphones to phase-average the PIV images or perform time-resolved measurements.

An interesting finding from the phase-averaged FOV is that the intensity of wall-normal fluctuations was generally higher upstream of the array than downstream. This trend was observed in both configurations and is consistent with the previous observations of wall-normal Reynolds stress in the mean fields, suggesting a possible evolution of the interaction between the array and the turbulent boundary layer along the streamwise direction.

On the other hand, the amplitude of the phase-averaged wall-normal velocity fluctuations, box-averaged in the vicinity of the resonator's orifice, was higher in the downstream resonator than in the upstream one of the array. This result is promising, as it suggests that the resonators exhibit different behavior across the array. Additionally, a lower amplitude of the wall-normal velocity fluctuations was observed when the velocity was phase-averaged using the sub-resonance frequency. This finding is consistent with the results from Hassanein et al. (2024) for the single resonator configuration. The final interesting result, from the box-averaging of the phase-averaged fluctuating wall-normal velocity, is the difference in phase shift between the velocity and the cavity pressure in the first resonator compared to the last one. This suggests that using an array of resonators, instead of a single resonator, can alter the impedance of the resonator when the sub-resonance frequency is considered.

Chapter 7

Conclusion

Helmholtz resonators under a turbulent boundary layer have been the subject of numerous studies over the past decades. However, only the works of Dacome et al. (2024) and Hassanein et al. (2024) have demonstrated the potential of small-scale resonators ($d^+ \approx 60$) as meta-units for passive surface modifications aimed at manipulating wall shear stress. In this study, a bi-dimensional array of small-scale Helmholtz resonators was analyzed under a turbulent boundary layer. The experimental setup was designed to maximize the interaction between the array and the turbulent boundary layer. It was constructed using an anodized aluminum top plate and 3D-printed boxes housing the resonators' cavities. Two different configurations were manufactured and tested: the first with a streamwise spacing between the spanwise rows of resonators of $\Delta x_1^+ = 250$, and the second with $\Delta x_2^+ = 500$. Configuration 1 exhibited more promising results than configuration 2, suggesting that further measurements and analysis could be beneficial for this setup.

To gain a complete understanding of the impact of an array of small-scale Helmholtz resonators on a turbulent boundary layer, various measurements and analyses were conducted. The study began by examining the resonators' response to turbulent boundary layer flow excitation using data from microphones embedded in the resonator cavities. The mean streamwise velocity profiles in the wake of the arrays were then analyzed through hot-wire anemometry, followed by a spectral analysis to evaluate the energy content of the streamwise velocity fluctuations. Additionally, PIV images were utilized to visualize the mean flow fields near the resonator orifices and to assess the periodic behavior of the flow above the array through phase-averaging based on microphone signals. Lastly, the skin friction coefficients in the wake of the arrays were determined at different streamwise positions using various computational methods.

The results are finally summarized and discussed in Chapter 6, confirming that small-scale Helmholtz resonators could serve as potential meta-units for flow control. This conclusion is supported by the clear differences observed in the mean flow compared to the baseline case, as well as the findings from the spectral analysis, which demonstrate that the resonator array modifies the energy distribution across different scales in the flow.

Nevertheless, this research did not yield new insights into the mechanism governing the interaction between an array of Helmholtz resonators and the turbulent boundary layer. Further studies are needed to achieve a deeper understanding of this interaction. Time-resolved measurements using the same setup could help explore why the first resonator in the array behaves differently from the last. Balance measurements on the experimental setup could assess whether embedding an array of Helmholtz resonators on a flat surface leads to a reduction in drag. Finally, direct measurements of wall-shear stress in the wake of the array, using oil film interferometry, could provide further insights into the cause of this attenuation.

Bibliography

M. Alster. Improved calculation of resonant frequencies of helmholtz resonators. *Journal of Sound and Vibration*, 24(1):63–85, 1972. doi: 10.1016/0022-460X(72)90123-X. URL https://www.sciencedirect.com/science/article/pii/0022460X7290123X.

J. D. Anderson. Fundamentals of aerodynamics. 1984. ISSN 0001-1452. doi: 10.2514/152157.

Christophe Bailly and Genevive Comte-Bellot. *Turbulence*. Springer Publishing Company, Incorporated, 2015. ISBN 3319161598.

Francis H. Clauser. The turbulent boundary layer. *Advances in Applied Mechanics*, 4:1–51, 1956. doi: 10.1016/S0065-2156(08)70370-3.

G Dacome, R Siebols, and WJ Baars. Small-scale helmholtz resonators with grazing turbulent boundary layer flow. *Journal of Turbulence*, page 2412586, 2024.

Kevin P. Flynn, Ronald L. Panton, and David G. Bogard. The effect of a row of helmholtz resonators on the turbulence of a boundary layer. In *27th Aerospace Sciences Meeting*. American Institute of Aeronautics and Astronautics, 1989. doi: 10.2514/6.1989-961. URL https://arc.aiaa.org/doi/10.2514/6.1989-961.

Farzin Ghanadi, Maziar Arjomandi, Ben Cazzolato, and Anthony Zander. Interaction of a flow-excited helmholtz resonator with a grazing turbulent boundary layer. *Experimental Thermal and Fluid Science*, 58:78–89, 2014. doi: 10.1016/j.expthermflusci.2014.06.016. URL https://digital.library.adelaide.edu.au/dspace/handle/2440/85532.

Abdelrahman Hassanein, Davide Modesti, Fulvio Scarano, and Woutijn J. Baars. Interaction of an inner-scaled helmholtz resonator with boundary-layer turbulence. *Phys. Rev. Fluids*, 9:114610, Nov 2024. doi: 10.1103/PhysRevFluids.9.114610. URL https://link.aps.org/doi/10.1103/PhysRevFluids.9.114610.

Nicholas Hutchins and Ivan Marusic. Evidence of very long meandering features in the logarithmic region of turbulent boundary layers. *Journal of Fluid Mechanics*, 579:1–28, 2007.

K. Uno Ingard. On the theory and design of acoustic resonators. *The Journal of the Acoustical Society of America*, 25(6):1037–1061, 1953. doi: 10.1121/1.1907220. URL https://doi.org/10.1121/1.1907220.

Lawrence E. Kinsler, Austin R. Frey, Alan B. Coppens, and James V. Sanders. *Fundamentals of Acoustics.* Wiley, New York, 4th edition, 1999. ISBN 978-0-471-84789-2.

Myoungkyu Lee and Robert D Moser. Direct numerical simulation of turbulent channel flow up to. *Journal of fluid mechanics*, 774:395–415, 2015.

C. Liu and D. F. Gayme. An input–output based analysis of convective velocity in turbulent channels. *Journal of Fluid Mechanics*, 888:A32, 2020.

Jens M Österlund, Arne V Johansson, Hassan M Nagib, and Michael H Hites. A note on the overlap region in turbulent boundary layers. *Physics of Fluids*, 12(1): 1–4, 2000.

Ronald L. Panton. Overview of the self-sustaining mechanisms of wall turbulence, 2001. ISSN 03760421.

Ronald L. Panton and John M. Miller. Excitation of a helmholtz resonator by a turbulent boundary layer. *The Journal of the Acoustical Society of America*, 58 (4):800–806, 1975. doi: 10.1121/1.380726. URL `https://doi.org/10.1121/1.380726`.

Ronald L. Panton, Kevin P. Flynn, and David G. Bogard. Control of turbulence through a row of helmholtz resonators. In *25th AIAA Aerospace Sciences Meeting*. American Institute of Aeronautics and Astronautics, 1987. doi: 10.2514/6.1987-436. URL `https://arc.aiaa.org/doi/10.2514/6.1987-436`.

Marc Perlin, David R Dowling, and Steven L Ceccio. Freeman scholar review: passive and active skin-friction drag reduction in turbulent boundary layers. *Journal of Fluids Engineering*, 138(9):091104, 2016.

Stephen B Pope. Turbulent flows. turbulent flows, by stephen b. pope, 2000.

Nicolas Renard and Sébastien Deck. A theoretical decomposition of mean skin friction generation into physical phenomena across the boundary layer. *Journal of Fluid Mechanics*, 790, 2016. ISSN 14697645. doi: 10.1017/jfm.2016.12.

Osborne Reynolds. Iv. on the dynamical theory of incompressible viscous fluids and the determination of the criterion. *Philosophical transactions of the royal society of london.(a.)*, (186):123–164, 1895.

Stephen K. Robinson. Coherent motions in the turbulent boundary layer. *Annual Review of Fluid Mechanics*, 23, 1991. ISSN 00664189. doi: 10.1146/annurev.fl.23.010191.003125.

Hermann Schlichting and Klaus Gersten. *Boundary-Layer Theory.* 2016. doi: 10.1007/978-3-662-52919-5.

Anton Silvestri, Farzin Ghanadi, Maziar Arjomandi, Benjamin Cazzolato, Anthony Zander, and Rey Chin. Mechanism of sweep event attenuation using micro-cavities in a turbulent boundary layer. *Physics of Fluids*, 30(5):055108, 05 2018. ISSN 1070-6631. doi: 10.1063/1.5026130. URL `https://doi.org/10.1063/1.5026130`.

Alexander J Smits, Beverley J McKeon, and Ivan Marusic. High–reynolds number wall turbulence. *Annual Review of Fluid Mechanics*, 43(1):353–375, 2011.

James M. Wallace. Quadrant analysis in turbulence research: History and evolution. *Annual Review of Fluid Mechanics*, 48, 2016. ISSN 00664189. doi: 10.1146/annurev-fluid-122414-034550.